



Deposited via The University of Leeds.

White Rose Research Online URL for this paper:

<https://eprints.whiterose.ac.uk/id/eprint/222062/>

Version: Published Version

Article:

Chen, J., Song, S.-S., Ye, J. et al. (2024) Axial compressive behaviour and design of concrete-filled wire arc additively manufactured steel tubes. *Structures*, 70. 107495. ISSN: 2352-0124

<https://doi.org/10.1016/j.istruc.2024.107495>

This is an author produced version of an article published in *Structures*, made available under the terms of the Creative Commons Attribution License (CC BY), which permits unrestricted use, distribution and reproduction in any medium, provided the original work is properly cited.

Reuse

This article is distributed under the terms of the Creative Commons Attribution (CC BY) licence. This licence allows you to distribute, remix, tweak, and build upon the work, even commercially, as long as you credit the authors for the original work. More information and the full terms of the licence here:

<https://creativecommons.org/licenses/>

Takedown

If you consider content in White Rose Research Online to be in breach of UK law, please notify us by emailing eprints@whiterose.ac.uk including the URL of the record and the reason for the withdrawal request.

Axial Compressive Behaviour and Design of Concrete-filled Wire Arc Additively Manufactured Steel Tubes

Ju Chen¹, Sha-Sha Song¹, Jun Ye^{1*}, Guan Quan¹, Pinelopi Kyvelou², Leroy Gardner²

1. Institute of Structural Engineering, Zhejiang University, Hangzhou, Zhejiang, China

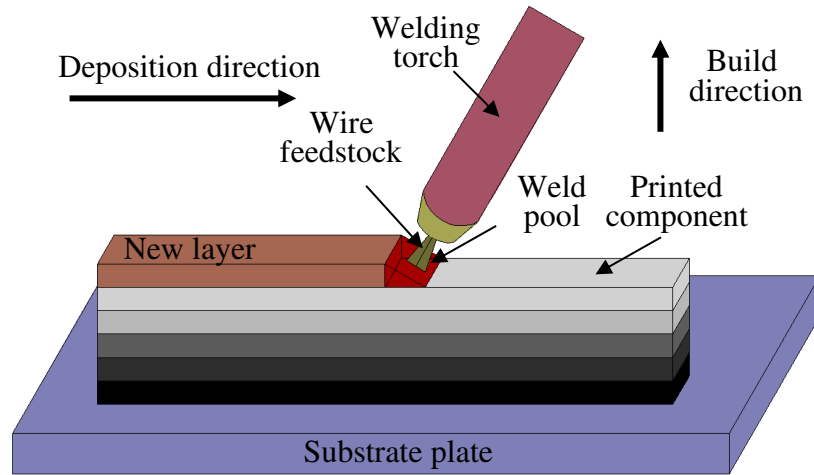
2. Department of Civil and Environmental Engineering, Imperial College London, London, UK

Abstract: The axial compressive behaviour of concrete-filled wire arc additively manufactured (WAAM) steel tubular columns is investigated experimentally in this paper. Firstly, the manufacture of a series of WAAM steel plates and tubes is described. The results of tensile testing performed on coupons cut from the WAAM plates, to obtain the mechanical properties of the printed material, are summarised. 3D laser scanning was employed to generate digital models and to capture the geometric features of the WAAM steel test specimens. Concrete was then cast into the WAAM steel tubes, creating a total of nine concrete-filled steel tubular (CFST) specimens of different diameters, thicknesses and lengths that were subjected to compressive loading. The axial compressive load-deformation responses and ultimate loads of the specimens were obtained and the influence of the as-built surface undulations of the WAAM sections was assessed. Comparisons of the test results against existing structural design provisions highlight the need to consider the influence of the weakening effect of the geometric undulations that are inherent to the WAAM process on the structural response of CFST sections, in order to achieve safe-sided strength predictions.

Keywords: 3D printing; Axial compressive behaviour; Concrete-filled steel tube (CFST); Experiments; Laser Scanning; Testing; Ultimate load; Wire arc additive manufacturing (WAAM).

24 **1. INTRODUCTION**

25 Recent developments in the directed energy deposition (DED) methods of additive manufacturing
26 (AM) have led to growing interest in and increasing usage of this technology in the construction sector
27 [1]. DED methods offer several advantages over other AM methods for constructional applications, such
28 as relatively low cost, reasonable manufacturing times and essentially unlimited build sizes [2-6].



29

30 Figure 1. Schematic diagram of WAAM process

31 Among the various metal DED technologies, wire arc additive manufacturing (WAAM), which
32 uses conventional welding technology, coupled with robotic control, is emerging as the method of
33 choice for large scale applications [1,7-17], and is the focus of the present paper. As shown in Fig. 1,
34 during the WAAM process, wire feedstock is melted and deposited onto a substrate plate in a layer by
35 layer fashion. WAAM has the potential to have a significant impact on the construction industry; an
36 early example of this potential is the MX3D bridge constructed by the Dutch company MX3D
37 (www.mx3d.com). With its construction being beyond the scope of current design specifications [18-
38 21], this novel structure required extensive experimental and numerical research for its safety
39 assessment. A comprehensive series of experiments was thus conducted, involving material testing
40 [14,22,23], cross-section testing [24] and full structural testing [25]; numerical simulations were also
41 carried out [25]. Research into the performance of metal additively manufactured components with a
42 structural engineering focus has been increasing in recent years [1]. Studies into the behaviour of
43 structural elements produced by powder bed fusion (PBF) have been reported in [26,27], while

44 investigations into WAAM structural elements have been presented at the material level [14,27-31], the
45 cross-section level [32,33], the member level [34,35] and the system level [6]. The latter system level
46 study involved the optimisation [6], testing [36] and environmental impact assessment [37] of a series
47 of 2 m span WAAM tubular trusses, an example of which is shown in Fig. 2. The use of WAAM for
48 hybrid construction has also been explored, including recent studies into the structural behaviour of hot-
49 rolled I-sections strengthened by the addition of WAAM material at the flange tips [38,39].

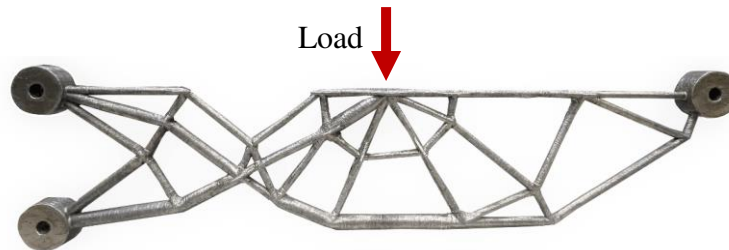


Figure 2. Optimised WAAM tubular truss [36]

50 Concrete-filled steel tubular (CFST) elements are widely used in construction applications [40-47],
51 such as in arch bridges, high rising buildings and transmission towers. The combined effect of the steel
52 tube and the inner concrete leads to composite structural members of superior performance relative to
53 the sum of the component parts [40], with the inner concrete delaying the development of local buckling,
54 as well as the rise in temperature in the event of a fire, of the steel tube [40,45], and with the steel tube
55 enhancing the strength and ductility of the inner concrete through confinement action. The steel tube
56 also eliminates the need of formwork for concrete casting, resulting in fast-track construction. Surface
57 undulations are a natural characteristic of the WAAM process; in the context of CFST, there undulations
58 can enhance the interaction between the WAAM steel tube and the inner concrete, and hence improve
59 the structural performance [48]. Furthermore, unlike CFST members fabricated from conventional steel
60 tubes that have seam welds running along the length of the members where fracture is often observed
61 [49,50], the continuously printed ‘hoops’ for which the start and end points of each layer are offset
62 circumferentially forming the WAAM tubes, are expected to mitigate this issue, resulting in enhanced
63 ductility [51]. To date, research into the compressive behaviour of CFST members has been limited to
64 cross-sections comprising conventionally manufactured tubes [41-43,46,47], while the response of
65 CFST elements with WAAM tubes is still to be investigated. Seeking to bridge this gap, a series of axial

66 compressive tests on CFST sections with WAAM steel elements has been conducted and is presented
67 herein.

68 The process followed for the fabrication of the WAAM steel tubes is first presented, while the
69 methods adopted for the determination of the as-built geometric properties of the examined specimens,
70 featuring hand measurements, measurements based on Archimedes' principle and 3D laser scanning, are
71 described. The results of complementary material tests, undertaken for the determination of the mechanical
72 properties of the concrete and WAAM material, are then summarised. A description of the axial
73 compressive tests on the CFST specimens is provided, while the test results are analysed and discussed.
74 Finally, comparisons are made against the strength predictions yielded by current structural design
75 specifications [18,52-57], and the results highlight the need to consider the influence of the weakening
76 effect of the geometric undulations that are inherent to the WAAM process on the structural response of
77 CFST sections.

78 **2. MANUFACTURE OF WAAM ELEMENTS**

79 Nine WAAM steel tubes of three different nominal thicknesses and diameters, and of two different lengths
80 were manufactured for the compression tests, such that their nominal diameter to thickness ratios ranged
81 from 30 to 100 and their nominal length to diameter ratios varied between 3.3 and 6.7. Oval steel tubes
82 with flat sides and thicknesses of 3 mm and 6 mm were also manufactured, in order to obtain plates for
83 the extraction of tensile coupons. The labels employed for the WAAM steel tubes include information
84 regarding the diameter, thickness and length of the WAAM steel tube in mm. For example, Specimen
85 D240T3L600 is a WAAM steel tube with a nominal diameter D_n of 240 mm, a nominal thickness t_n of 3
86 mm and a nominal length L_n of 600 mm. For the tensile coupons, the identification system starts with the
87 letter "H" or "V" for the coupons extracted horizontally or vertically relative to the deposition direction
88 respectively, followed by the letter "A" or "M" for the coupons with their surface left in its as-built
89 undulating state or machined smooth respectively, and, finally, by the test number. For example, Specimen
90 H-A-1 is the first coupon with an as-built surface, extracted horizontally from within its parent plate, i.e.
91 at a 0° angle to the deposition direction.

92 Printing of a subset of the WAAM circular hollow sections (CHS) and oval tubes is shown in Fig. 3.

93 The WAAM components were manufactured using a welding torch attached to a 6-axis robotic arm and a
 94 metal inert gas (MIG) welding machine. The utilised shielding gas was a mixture of 97% Ar and 3% CO₂.
 95 The key parameters employed during the WAAM process are summarised in Table 1. The environmental
 96 temperature and humidity of the room were 12 °C to 21 °C and 35% to 55%, respectively. The components
 97 were printed layer-upon-layer, following the cross-section slice traces as defined in their digital models
 98 created in Rhino 3D [58]. The feedstock material was carbon steel welding wire ER50-6, which was
 99 deposited onto a Q235b steel substrate plate.

100 **Table 1** Process parameters used for WAAM specimens

Nominal thickness (mm)	Welding speed (m/min)	Wire feed rate (m/min)	Deposition rate (kg/h)	Wire feedstock diameter (mm)	Current (A)	Arc voltage (V)	Layer thickness (mm)
3	0.75	4	0.5-2	1.2	100-140	18-23	1.8
4	0.65-0.70	4	0.5-2	1.2	100-140	18-23	1.8
6	0.55-0.60	6.2-6.5	0.5-2	1.2	100-140	18-23	2.0

101 Following their fabrication, the WAAM CHS and oval tubes were detached from their substrate plates
 102 using a plasma arc cutter. Note that a minimum distance equal to the outer diameter of the steel tube was
 103 maintained between the base plate and the cutting line, to eliminate the influence of any initial printing
 104 defects on the performance of the WAAM components. Both ends of the WAAM steel tubes were
 105 machined to be flat and parallel and their exterior surfaces were sandblasted with glass beads to remove
 106 any welding soot from the WAAM process.



(a) WAAM CHS for compression tests



(b) WAAM oval tubes with flat sides for tensile coupon tests

Figure 3. Printing of subset of WAAM CHS and oval tubes

107 **3. GEOMETRIC MEASUREMENTS**

108 The geometric characteristics of WAAM steel tubes are more variable than those of rolled sections due
109 to the surface undulations arising from the printing process, rendering the use of conventional measuring
110 techniques impractical. Thus, in order to obtain the as-built geometric properties of the WAAM steel
111 tubes, three measuring methods were employed, featuring hand measurements, measurements based on
112 Archimedes' principle and 3D laser scanning. The details of each method, as well as the obtained results,
113 are discussed and compared in this section.

114 **3.1. Hand measurements**

115 A digital micrometre with an accuracy of 0.001 mm and a measuring tape were employed to provide
116 baseline geometric data for the as-built WAAM components. For the WAAM steel tubes, the wall
117 thickness t_h was determined as the average value of sixteen measurements taken at eight locations
118 equally spaced around the section perimeter at both ends, utilising the digital micrometre - see Fig. 4(a).
119 Similarly, measurements of the average perimeter C_h of the outer surface of each steel tube were taken
120 at five locations evenly distributed along the member length, and their mean value was used to determine
121 the average outer diameter $D_h = C_h/\pi$. Finally, the length L_h of each steel tube was determined based on
122 four length measurements, taken at the locations indicated in Fig. 4(a). The average geometric properties
123 of the steel tubes, as determined by the hand measurements, are listed in Table 2; the nominal thickness
124 t_n , nominal diameter D_n and nominal length L_n of each WAAM steel tube are also provided in Table 2. A_h
125 is the cross-sectional area and V_h is the volume calculated using the reported measured values. For the
126 WAAM tensile coupons, the average width $b_{C,h}$ and thickness $t_{C,h}$ were determined based on hand
127 measurements taken with the digital micrometre at eight locations evenly distributed along the parallel
128 length of each coupon - see Fig. 4(b). The average values of $b_{C,h}$ and $t_{C,h}$, along with the average cross-
129 sectional area $A_{C,h}$ of each coupon are listed in Table 3. The nominal widths and thickness of the
130 coupons, $b_{C,n}$ and $t_{C,n}$, respectively, are also provided in the table. In the present study, coupons with a
131 nominal thickness of 6 mm were tested, while tests on corresponding 3 mm coupons have been reported
132 in [15,59].

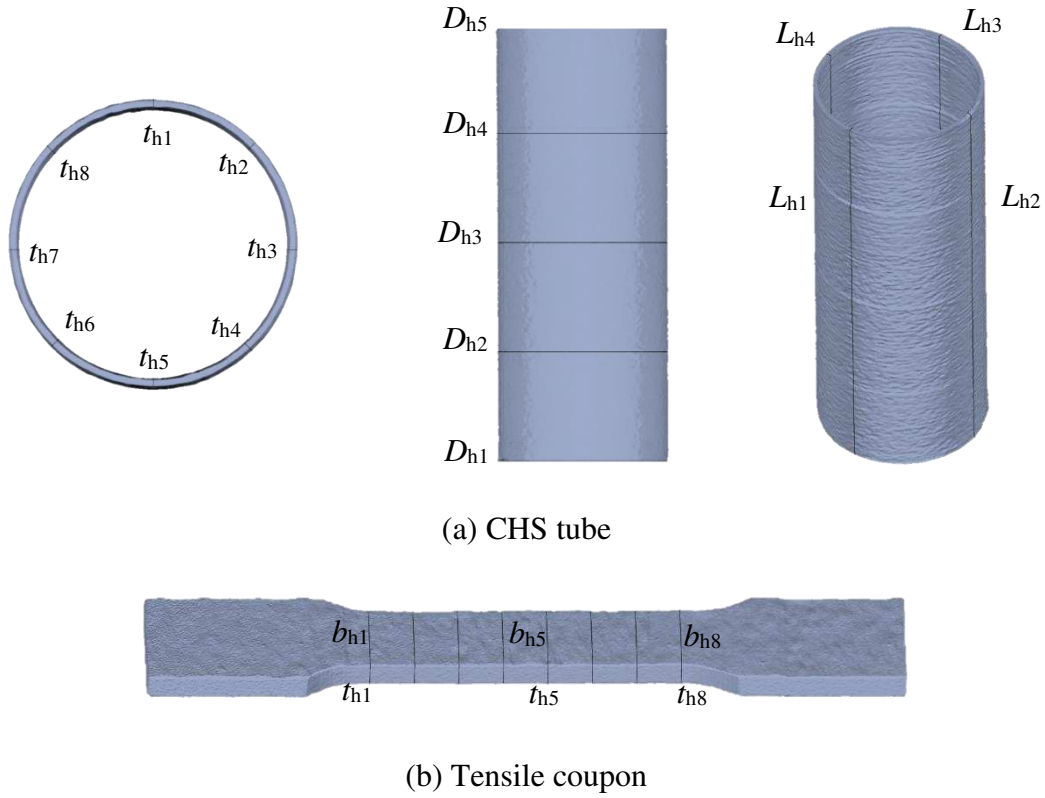


Figure 4. Locations of hand measurements for WAAM specimens

133 **3.2. Measurements based on Archimedes' principle**

134 Archimedes' principle, which is frequently employed for the determination of the porosity of concrete
 135 elements [60,61], was employed herein for the calculation of the density of the WAAM material and
 136 subsequently, the volume of the WAAM steel components. First, an electronic balance was used to
 137 weigh the WAAM tensile coupons and tubes (with their masses labelled $m_{C,Arch}$ and m_{Arch} respectively),
 138 as shown in Fig. 5(a). A cylinder was then utilised to measure the volume of the tensile coupons $V_{C,Arch}$
 139 based on the water displacement method, as illustrated in Fig. 5(b), which allowed the determination of
 140 the density $\rho_{C,Arch}$ of each coupon, in line with Eq. (1).

141
$$\rho_{C,Arch} = \frac{m_{C,Arch}}{V_{C,Arch}} \quad (1)$$

142 Finally, the average density $\rho_{C,Arch}$ of all coupons, which was 7903 kg/m^3 , was used for the
 143 determination of the volume V_{Arch} of the steel tubes, based on their measured mass m_{Arch} . The measured
 144 geometric properties of the WAAM steel tubes and steel coupons are reported in Tables 2 and 3,

145 respectively.



(a) Electronic balance

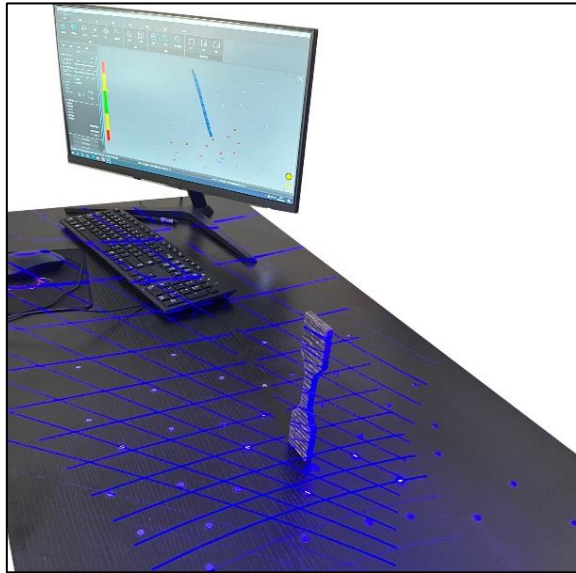


(b) Measuring cylinder

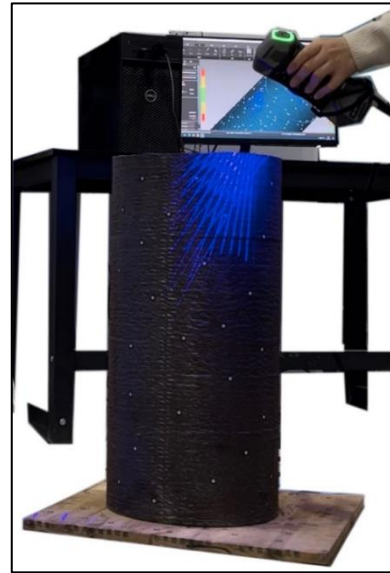
Figure 5. Equipment used for Archimedes' measurements

146 3.3. 3D laser scanning

147 3D laser scanning was employed to capture digitally the full geometry of the WAAM steel components
148 prior to testing. A SCANTECH 3D laser scanner, capable of capturing up to 500,000 points per second
149 with an accuracy of 0.05 mm, was employed to scan all the WAAM steel tubes and coupons. The
150 acquired point cloud data were processed using the software Scanviewer. Following calibration of the
151 scanner, markers were attached to the surfaces of the WAAM steel tubes and a flat plate on which the
152 specimens were placed during scanning, to facilitate alignment of the relative coordinate systems of the
153 3D point clouds during the coordinate conversion process. At least three markers need to be shared
154 between adjacent scan views for merging to be realised.

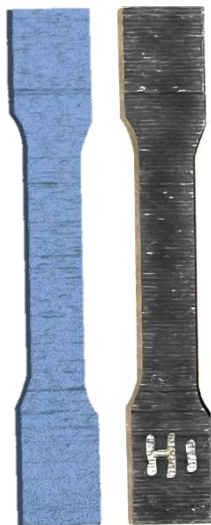


(a) Typical coupon



(b) Typical steel tube

Figure 6. 3D laser scanning of WAAM specimens



(a) Coupon



(b) Steel tube

Figure 7. Comparisons of scanned surface profiles with respective specimens

155 The surface profiles of all steel coupons, as well as the outer surface profiles of the four steel tubes
 156 (namely D240T3L600, D240T6L600, D300T3L600 and D300T6L600), were obtained with one
 157 continuous scan, as shown in Fig. 6. Typical comparisons between scanned surface morphologies and
 158 the respective WAAM components are shown in Fig. 7. The scanned 3D models (.stl) were subsequently
 159 imported into the software Geomagic Wrap [62], for determination of their geometry. The volumes of
 160 the WAAM steel tubes V_{Scan} and steel coupons $V_{C,Scan}$, as determined from the laser scans, are reported
 161 in Tables 2 and 3, respectively.

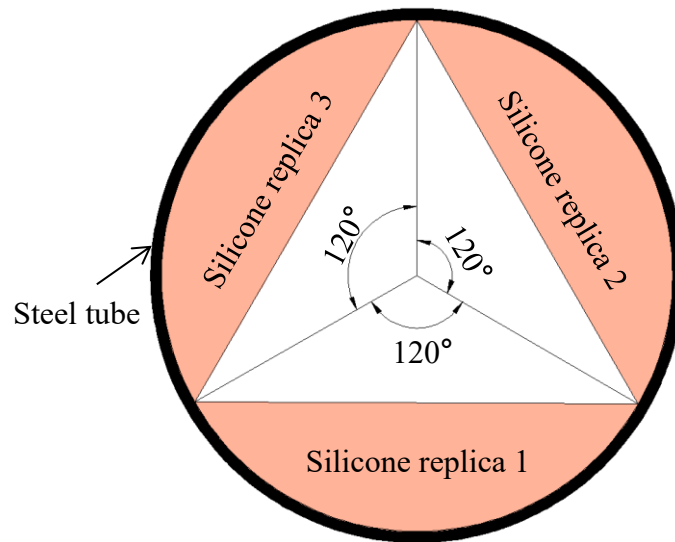


Figure 8. Illustration of silicone replicas of inner surface of tubes

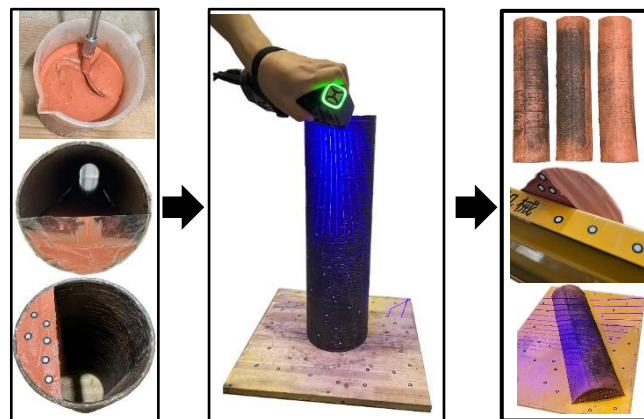
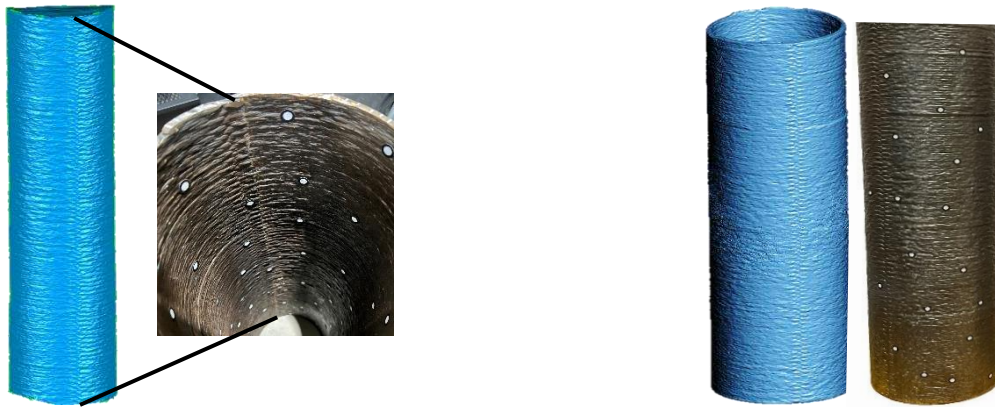


Figure 9. Production and scanning of silicone casts

162 The proportions of the WAAM steel tubes D180T3L600 and D180T6L600 were such that scanning
 163 of the full inner surface profiles just from the two tube ends was not possible. Silicone casting was
 164 therefore undertaken to form silicone replicas of the inner tube surface that could subsequently be
 165 scanned [12]. In order to reduce the volume of silicone and facilitate removal of the silicone casts from
 166 within the WAAM steel tubes, three moulds were created, as illustrated in Fig. 8, while silicone release
 167 spray was applied to the inner tube surface. The prepared silicone mixture was slowly poured into the
 168 tubes and allowed to set for at least 24 hours. Following setting, at least three markers were positioned
 169 on each end of the silicone casts, as shown in Fig. 9, which were scanned together with the WAAM
 170 tubes. The silicone casts were then removed from within the steel tubes and scanned individually. Finally,
 171 the scans of the outer and inner tube surfaces were merged and converted into a complete 3D model. A
 172 typical comparison between the scan of a silicone cast and the respective inner surface profile of a

173 WAAM steel tube is shown in Fig. 10(a), while a typical outer surface comparison is shown in Fig.
174 10(b). Their geometric dimensions are summarised in Table 2.



(a) Inner surface of specimen D180T6L600

(b) Outer surface of specimen D180T6L600

Figure 10. Typical comparisons of scanned surface profiles

175 Capturing the inner surface geometries of the WAAM steel tubes D180T4L1200, D240T4L1200
176 and D300T4L1200 was not practically possible even with silicone casting, due to their length. The
177 average thicknesses and cross-sectional areas of these specimens were therefore determined based on
178 the Archimedes' measurements.

Table 2 Average measured geometric properties of WAAM steel tubes

Steel tube ID	t_n (mm)	D_n (mm)	L_n (mm)	t_h (mm)	D_h (mm)	L_h (mm)	A_h (mm ²)	V_h (mm ³)	m_{Arch} (kg)	V_{Arch} (mm ³)	V_{Scan} (mm ³)	$\frac{V_h}{V_{Arch}}$	$\frac{V_{Scan}}{V_{Arch}}$
D180T3L600	3	180	600	2.91	179.68	617.4	1618.2	999×10^3	8.05	1019×10^3	990×10^3	0.98	0.97
D240T3L600	3	240	600	3.10	238.94	611.3	2295.4	1402×10^3	10.75	1360×10^3	1374×10^3	1.03	1.01
D300T3L600	3	300	600	3.13	299.87	614.9	2913.3	1787×10^3	13.35	1689×10^3	1702×10^3	1.06	1.01
D180T6L600	6	180	600	6.58	179.54	611.1	3577.5	2184×10^3	16.65	2107×10^3	2147×10^3	1.04	1.02
D240T6L600	6	240	600	6.46	239.66	608.3	4730.6	2873×10^3	22.15	2803×10^3	2863×10^3	1.03	1.02
D300T6L600	6	300	600	6.54	298.97	609.6	6007.4	3658×10^3	27.75	3511×10^3	3580×10^3	1.04	1.02
D180T4L1200	4	180	1200	3.69	179.63	1219.9	2039.6	2482×10^3	19.10	2417×10^3	-	1.03	-
D240T4L1200	4	240	1200	3.79	239.85	1219.4	2810.7	3428×10^3	25.45	3220×10^3	-	1.06	-
D300T4L1200	4	300	1200	3.82	299.95	1210.8	3553.8	4292×10^3	31.75	4018×10^3	-	1.07	-
											Mean	1.04	1.01
											CoV	0.026	0.018

Table 3 Average measured geometric properties of WAAM steel coupons

Coupons		$b_{C,n}$	$t_{C,n}$	$b_{C,h}$	$t_{C,h}$	$A_{C,h}$	$m_{C,Arch}$	$V_{C,Arch}$	$V_{C,Scan}$	$\rho_{C,Arch}$	$\frac{V_{C,Scan}}{V_{C,Arch}}$
		(mm)	(mm)	(mm)	(mm)	(mm ²)	(g)	(mm ³)	(mm ³)	(kg/m ³)	
As-built steel	H-A-1	20	6	20.66	6.17	127.42	220.47	28000	27910	7873.9	1.00
	H-A-2	20	6	20.29	5.98	121.20	224.77	29000	28650	7750.7	0.99
	H-A-3	20	6	20.31	6.17	125.20	221.43	28500	28160	7769.5	0.99
	V-A-1	20	6	20.19	6.16	124.30	227.48	29000	28890	7844.1	1.00
	V-A-2	20	6	19.99	6.28	125.57	227.26	29000	28730	7836.6	0.99
	V-A-3	20	6	20.40	6.19	126.20	223.73	27500	27220	8135.6	0.99
Machined steel	H-M-1	20	6	20.47	5.31	108.67	196.09	25000	24570	7843.6	0.98
	H-M-2	20	6	20.32	5.11	103.96	185.30	23500	23070	7885.1	0.98
	V-M-1	20	6	20.24	5.37	108.73	195.98	24500	24280	7999.2	0.99
	V-M-2	20	6	20.05	4.78	95.99	169.90	21000	20980	8090.5	1.00
									Mean	7902.9	0.99
									CoV	0.016	0.006

183

Table 4 Summary of average geometric properties and key test results of concrete-filled WAAM steel tubes, as determined by laser scanning

WAAM steel Tube ID	t (mm)	D (mm)	L (mm)	A (mm ²)	A_c (mm ²)	$N_{u,Exp}$ (kN)	$\delta_{V,u}$ (mm)	$\delta_{H,u}$ (mm)	DI	$\frac{A}{A_{min}}$	$\frac{A}{A_{max}}$	$\frac{A_{sd}}{A}$
D180T3L600	2.89	178.08	617.2	1590.6	23316.3	1904	3.03	a	6.25	1.08	0.91	0.028
D240T3L600	3.00	237.94	610.9	2214.3	42251.4	3010	2.84	a	7.06	1.06	0.92	0.034
D300T3L600	3.06	295.23	614.5	2804.2	65651.7	4274	2.47	a	4.50	1.03	0.94	0.029
D180T6L600	6.44	178.46	615.6	3477.7	21535.7	2428	2.97	a	5.39	1.05	0.96	0.016
D240T6L600	6.40	238.19	608.1	4660.4	39898.7	3797	2.79	a	6.75	1.04	0.94	0.015
D300T6L600	6.47	297.90	609.3	5923.6	63776.1	5460	2.61	a	5.79	1.05	0.93	0.020
D180T4L1200	3.69 ^b	179.63 ^b	1219.9 ^b	2039.6 ^b	23302.8 ^b	2002	5.7	0.15	5.23			
D240T4L1200	3.79 ^b	239.85 ^b	1219.4 ^b	2810.7 ^b	42371.7 ^b	3208	5.46	0.61	5.39			
D300T4L1200	3.82 ^b	299.95 ^b	1210.8 ^b	3553.8 ^b	67108.5 ^b	4791	5.13	1.44	4.52			
									Mean	1.05	0.93	0.02
									CoV	0.019	0.017	0.328

184 Note: a signifies that for specimens with a length less than 1000 mm, their horizontal displacement was not measured; b signifies that the dimension of
185 the WAAM steel tube was determined by the Archimedes' measurements.

186 **3.4. Comparison between measuring methods**

187 The measured volumes of the WAAM steel tubes determined using the different measuring methods are
188 compared in Table 2. The volumes calculated using the hand measurements V_h differ somewhat from
189 those obtained based on Archimedes' principle V_{Arch} , with their deviation ranging between -2% and 7%.
190 On the contrary, the volumes V_{Scan} determined using the laser scans were very similar to those
191 determined using Archimedes' principle V_{Arch} , with the mean value of V_{Scan}/V_{Arch} ratio being 1.01 and
192 the coefficient of variation (CoV) being 0.018, providing confidence in the 3D laser scanning method.
193 Similar conclusions were drawn for the geometric properties of the tensile coupons, as reported in Table
194 3, with the mean value of $V_{C,Scan}/V_{C,Arch}$ being 0.99 and the CoV being 0.006.

195 Overall, 3D laser scanning is deemed to be the most suitable method for determining accurate
196 measurements of the geometry of the WAAM steel elements, while the hand and Archimedes'
197 measurements served as reference values for comparison and verification purposes.

198 **3.5. Analysis of cross-sectional geometry of WAAM components**

199 The 3D models of the WAAM steel components obtained from the laser scans were imported into Rhino
200 3D [65] for geometric analysis. Contouring of each component along its length was first undertaken, to
201 accurately determine the cross-sectional dimensions. Processing of typical WAAM components in
202 Rhino is shown in Fig. 11, where limited cross-sectional contours are presented for illustration purposes.

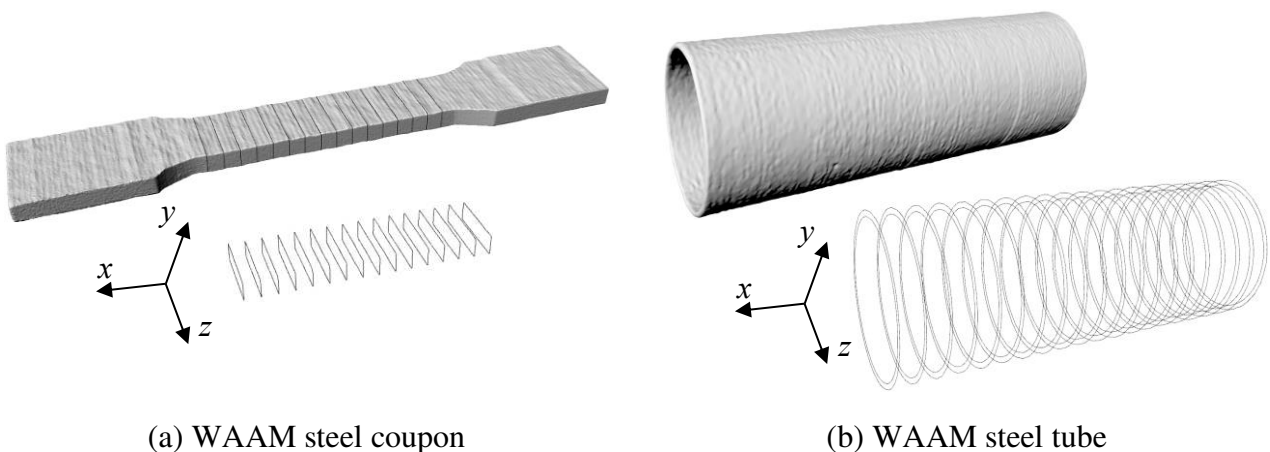


Figure 11. Scanned 3D model and cross-sectional contours of typical WAAM steel components

203 A sensitivity study was undertaken in order to determine the most suitable contour spacing for the
 204 examined WAAM steel components. Two typical WAAM elements (i.e. the WAAM coupon H-A-1 and
 205 the WAAM tube D180T6L600), were contoured at a spacing dx of 2.0 mm, 1.0 mm, 0.5 mm, 0.2 mm
 206 and 0.1 mm and their cross-sectional areas were subsequently determined. The obtained results are
 207 shown in Fig. 12, in which the mean, minimum and maximum values of the cross-sectional areas (A ,
 208 A_{\min} and A_{\max}) determined from the different contour spacings are normalised by the corresponding
 209 values determined using a contour spacing $dx = 0.1$ mm. As expected, the values of A_{\min} and A_{\max} were
 210 more sensitive to the contour spacing compared to the mean value of A . Since it was found that the
 211 cross-sectional areas obtained using a contour spacing $dx = 0.2$ mm were almost equal to those obtained
 212 with a contour spacing $dx = 0.1$ mm, a value of $dx = 0.2$ mm was adopted for the conducted geometric
 213 analyses. It should be noted that the adopted spacing of 0.2 mm was about 10% of the WAAM layer
 214 height, which was equal to approximately 2.0 mm, as shown in Fig. 13.

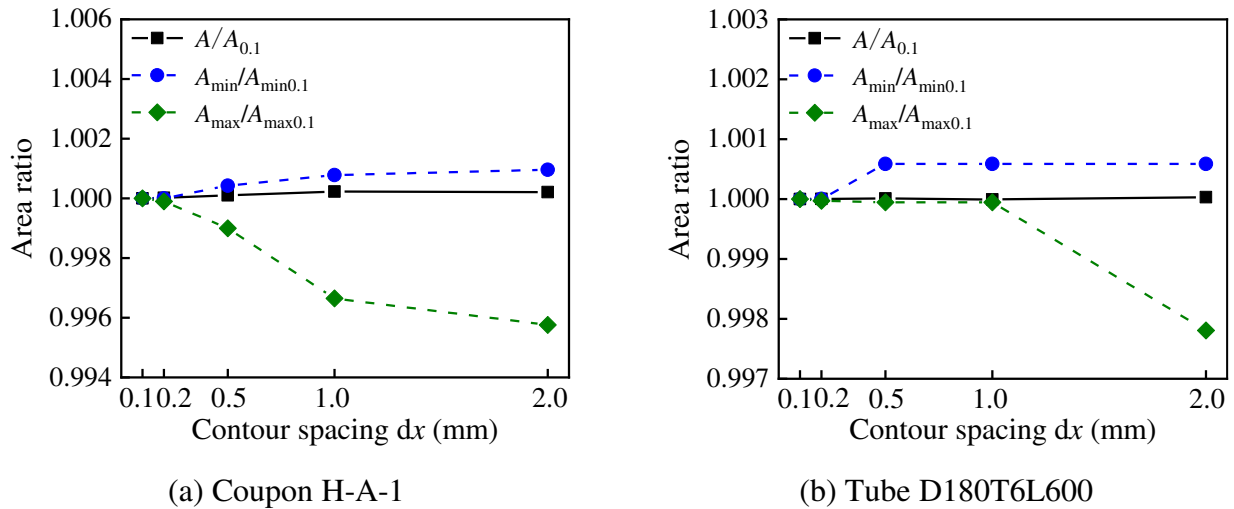


Figure 12. Sensitivity of cross-sectional area measurements to variation in contour spacing dx

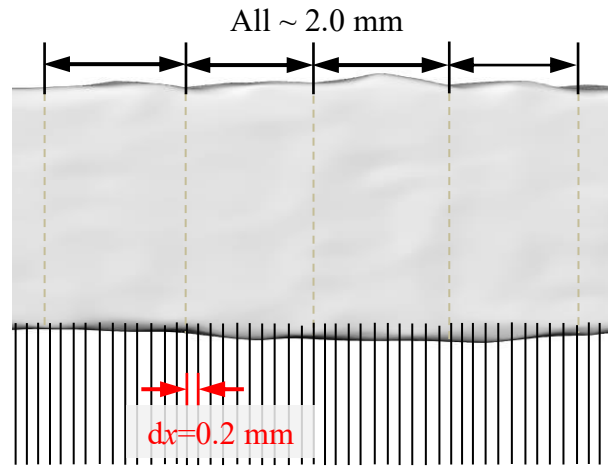


Figure 13. WAAM layer height (~ 2.0 mm) and adopted contour spacing dx of 0.2 mm

215 A summary of the geometric properties of the WAAM steel elements is reported in Tables 4 and 5,
 216 where t , D and L are the mean values of the wall thickness, outer diameter and length of the WAAM
 217 steel tubes, respectively, and A , A_{\min} and A_{\max} are the mean, minimum, and maximum values of the
 218 cross-sectional areas. Comparisons between the mean, minimum and maximum values through the ratio
 219 A/A_{\min} and A/A_{\max} are also presented in Tables 4 and 5. Reasonable differences (up to 4%) were
 220 observed between the A , A_{\min} and A_{\max} values of the same WAAM member, which are attributed to
 221 the undulations of the WAAM surface.

222 **Table 5** Summary of the geometric properties of the WAAM steel coupons as determined by the laser
 223 scanning

WAAM steel coupon ID	A (mm ²)	A_{\min} (mm ²)	A_{\max} (mm ²)	$\frac{A}{A_{\min}}$	$\frac{A}{A_{\max}}$	$\frac{A_{sd}}{A}$
H-A-1	123.67	119.62	128.52	1.03	0.96	0.014
H-A-2	124.46	123.24	127.04	1.01	0.98	0.014
H-A-3	123.22	122.56	126.25	1.01	0.98	0.013
H-M-1	108.67	107.44	110.21	1.01	0.99	0.012
H-M-2	103.96	101.74	105.22	1.02	0.99	0.012
V-A-1	124.52	119.57	129.11	1.04	0.96	0.018
V-A-2	124.86	120.23	129.09	1.04	0.97	0.016
V-A-3	124.84	119.81	129.29	1.04	0.97	0.017
V-M-1	108.73	106.49	109.73	1.02	0.99	0.011
V-M-2	95.99	93.15	97.09	1.03	0.99	0.010
			Mean	1.03	0.98	0.014
			CoV	0.013	0.012	-

224 The variation in the cross-sectional area for typical WAAM steel components (i.e. coupons V-A-1
 225 and H-A-1 and tubes D180T6L600 and D240T3L600) is shown in the histograms in Fig. 13, where each

226 cross-sectional area measurement A_i is normalised by the average cross-sectional area A of the
 227 corresponding WAAM specimen. The CoV values of the cross-sectional area, defined as the ratio of the
 228 standard deviation of the area to the average area i.e. A_{sd}/A of each component, are reported in Tables 4
 229 and 5. It can be seen that the values of A_{sd}/A range between 0.010 and 0.034, with the degree of dispersion
 230 decreasing with increasing thickness of the WAAM steel, as also reported by Kyvelou et al. [12].

231 The geometric dimensions of the WAAM steel tubes, determined as described above, were used
 232 for the subsequent analysis of the CFST specimens reported hereinafter. Exceptions to this are the larger
 233 (1200 mm) specimens, for which full laser scanning was not possible and thus the Archimedes'
 234 measurements were used – see Table 4, in which A_c is the mean cross-sectional area of the inner
 235 concrete, where the geometric dimensions, as well as the key test results, are provided.

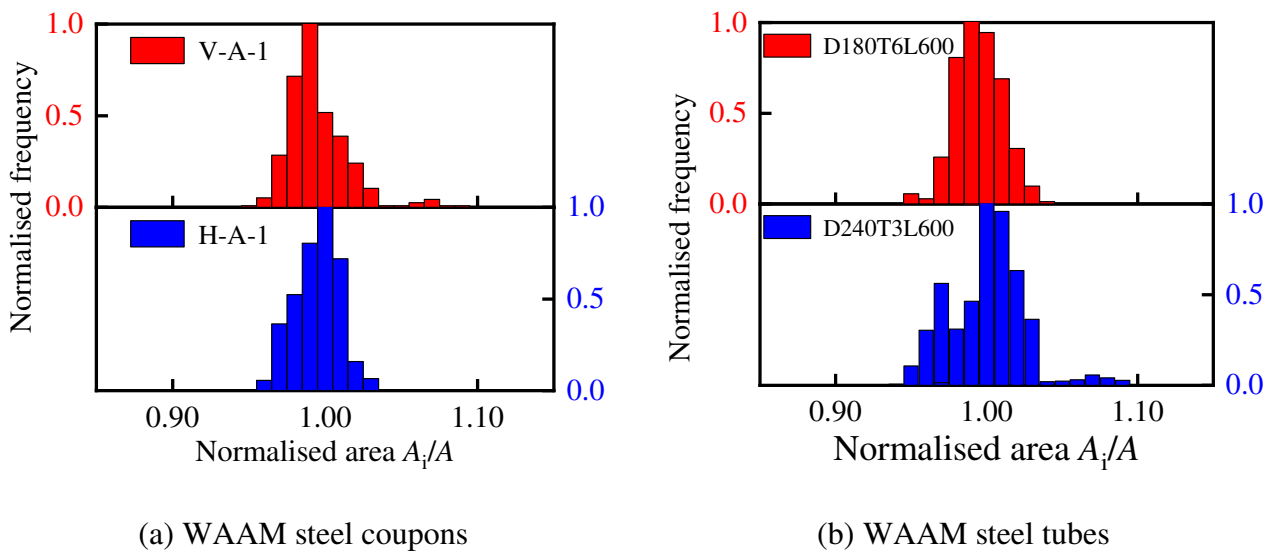


Figure 13. Distribution of normalised areas A_i/A of typical WAAM coupons and tubes

236 4. MATERIAL TESTS

237 4.1. Monotonic tensile tests

238 The material properties of the WAAM steel coupons, as well as their overall stress-strain response, were
 239 determined in compliance with GB/T 228.1-2010 [63]. The tensile coupons were extracted from the
 240 WAAM ovals at 0° and 90° to the deposition direction, as illustrated in Fig. 14, to assess the material
 241 anisotropy. Coupons of two different nominal thicknesses (i.e. 3 mm and 6 mm) were tested, while the

242 effect of the geometric undulations on the material properties was also investigated by comparing the
 243 response of as-built and machined coupons. In total, 20 tensile tests were conducted.

244 For the machined coupons, an electrical resistance strain gauge was attached at the mid-height on
 245 one side of each coupon to record longitudinal strains during the early stages of testing while, for both
 246 the machined and as-built coupons, an extensometer and a digital image correlation (DIC) system were
 247 employed to provide detailed measurements of the surface strain field throughout testing. Prior to testing,
 248 the parallel length of all coupons was painted white and then spray-painted with a random black speckle
 249 pattern, in order for the strains to be calculated over the full area of the parallel length. A 250 kN
 250 INSTRON testing machine operating in displacement control at a rate of 0.8 mm/min, was employed to
 251 apply the tensile load. The load, strain gauge and extensometer measurements were recorded at a
 252 frequency of 1 Hz, while the DIC system recorded the tensile force through an analogue to digital
 253 converter and the images at a frequency of 1 Hz.

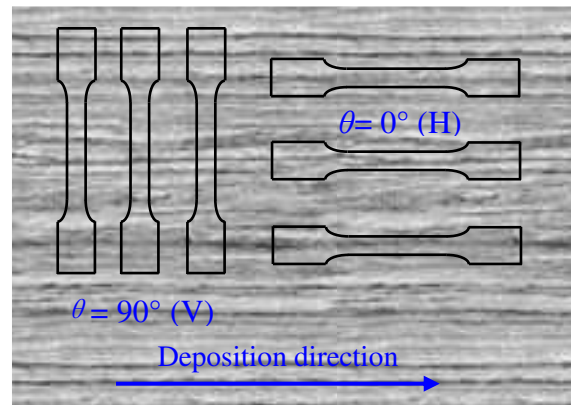


Figure 14. Orientation of tensile coupons extracted from WAAM plate relative to deposition direction

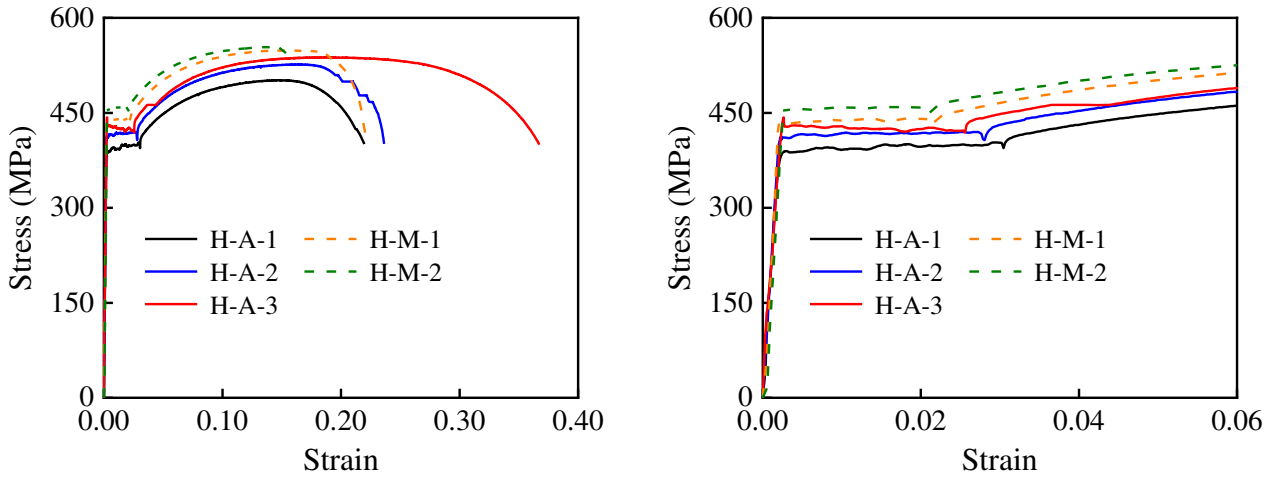
254

Table 6 Average material properties of WAAM steel coupons

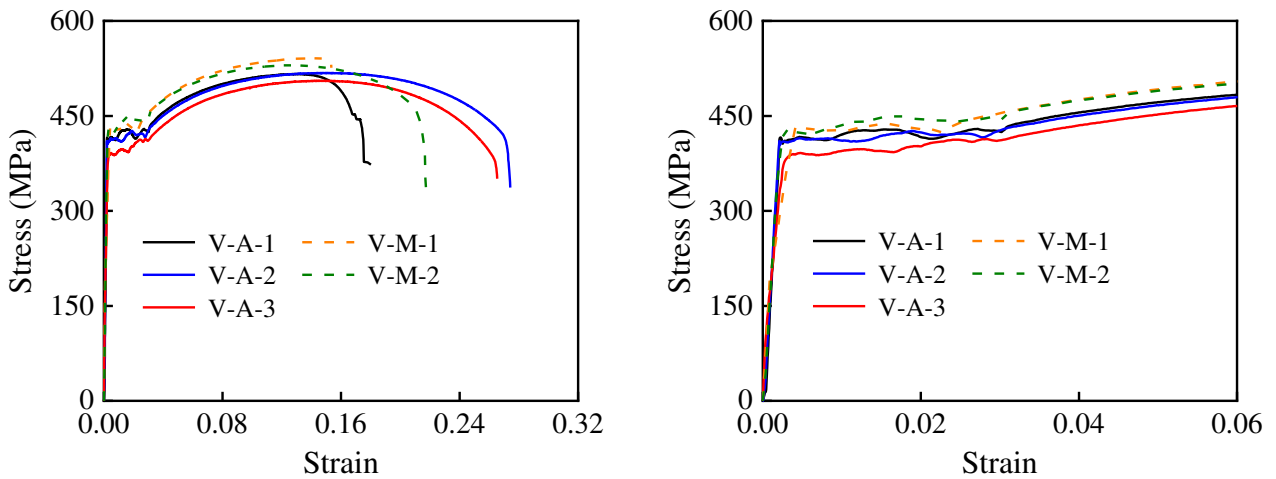
θ	$t_{C,n}$ (mm)	E (GPa)	f_y (MPa)	f_u (MPa)	ε_f	Surface
90°	6	205	405	513	0.20	As-built
		199	420	535	0.17	Machined
	3 ^[15,59]	198	408	515	0.09	As-built
0°	6	209	411	522	0.24	As-built
		199	445	551	0.18	Machined
	3 ^[15,59]	186	478	563	0.15	As-built

255 The obtained stress-strain curves for the 6 mm coupons are shown in Fig. 15, while a summary of
 256 the average material properties of the as-built and machined coupons, grouped by deposition direction

257 (i.e. 0° , and 90°), is reported in Table 6, where E is the Young's modulus, f_y is the yield strength, f_u is
 258 the ultimate tensile strength and ε_f is the fracture strain measured over the standard gauge length. Overall,
 259 the mechanical properties of the as-built coupons were found to be somewhat lower than those of the
 260 machined coupons, reflecting the negative influence of the WAAM surface undulations. Finally, mild
 261 anisotropy was observed, which was found to be more pronounced for the thinner coupons.



(a) Tensile coupons at 0° (H) to the deposition direction



(b) Tensile coupons at 90° (V) to the deposition direction

Figure 15. Stress-strain curves obtained from tensile tests on 6 mm coupons: full curve (left), initial range (right)

262 4.2. Concrete cube tests

263 Four concrete cubes were tested according to GB/T 50081-2002 [64] to obtain the material properties
 264 of the inner concrete. All tests were completed soon after the completion of the 28-day curing period.
 265 Based on the obtained test results, the mean compressive strength of the concrete was found to be
 266 $f_{cu} = 41.33$ MPa. Thus, the cylinder compressive strength of the inner concrete, which was used to

267 calculate the axial compressive strength of the concrete filled WAAM steel tube specimens, was taken
 268 as $f_c = 0.8f_{cu} = 33.06$ MPa [65], while the elastic modulus was taken as $E_c = 4730\sqrt{f_c} = 27200$ MPa
 269 [55].

270 5. AXIAL COMPRESSION TESTS ON CFST SPECIMENS

271 5.1. Specimen preparation and test setup

272 Following mixing, the concrete was cast into the WAAM steel tubes, and was allowed to cure for 28
 273 days. An end plate was welded to each end of the specimens to facilitate the application of the
 274 compressive force during testing and to ensure its even distribution. Nine CFST specimens were tested
 275 in total to investigate their mechanical behaviour under axial compression. The experimental layout
 276 adopted for the conducted tests is shown in Fig. 16. A 10,000 kN electric-hydraulic jack was used for
 277 the application of the axial load, operating at a constant displacement rate of 1 mm/min. Spherical hinge
 278 supports were employed at the specimen ends, with the distance between them considered as the
 279 effective length L_0 of the specimens - see Fig. 16. This setup has been successfully used in the past for
 280 CHS stub column tests [66,67]. Note that the geometric centroids of the ends of the specimens were
 281 aligned with the centroid of the spherical bearing to avoid eccentricity of loading.

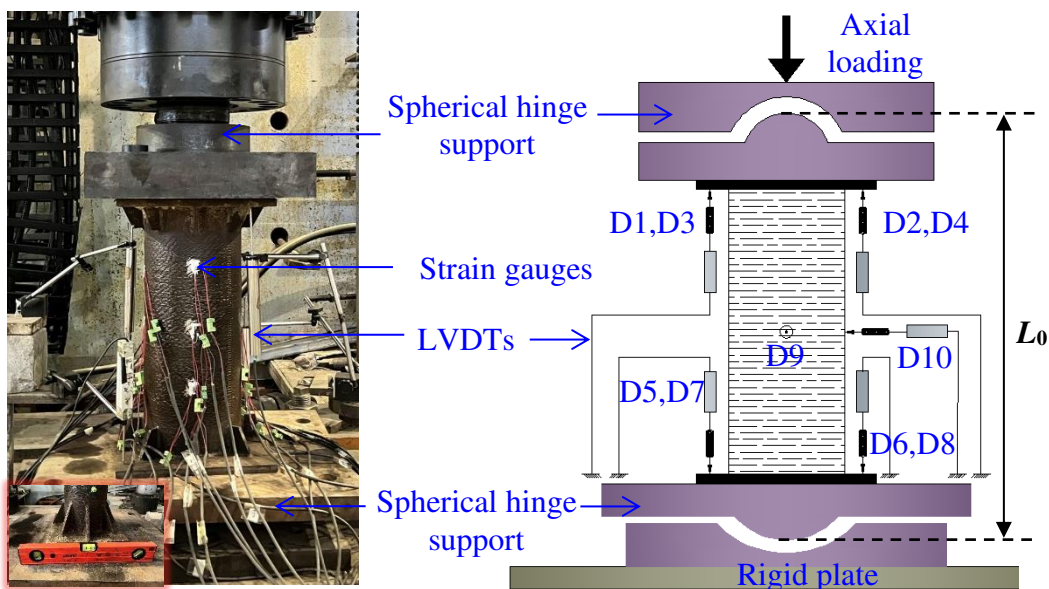


Figure 16. Test setup for axial compression tests on CFST specimens

282 5.2. Instrumentation

283 For the CFST specimens with a length of less than 1000 mm, eight LVDTs (D1-D8) were
 284 symmetrically positioned at both specimen ends to measure the vertical displacements (D1-D4 at the
 285 top end and D5-D8 at the bottom end), while, for the CFST specimens with a length of more than 1000
 286 mm, two additional LVDTs (D9 and D10) were used to measure the lateral displacements, as shown in
 287 Fig. 16. Twelve transverse and twelve longitudinal strain gauges (S_{T1} - S_{T12} and S_{L1} - S_{L12}) were attached
 288 to the CFST specimens at mid-height and the two 1/4-heights, as shown in Fig. 17, to measure the
 289 vertical and horizontal hoop strains. Prior to attaching the strain gauges, the surface of the WAAM steel
 290 tubes was locally sanded and polished to provide a smooth surface for adhesion. During testing, the load
 291 was stopped when the displacement of the load cell reached 80 mm. The load cell, LVDT and strain
 292 gauge readings were taken at a frequency of 1 HZ, using the DH3817 static data acquisition system.

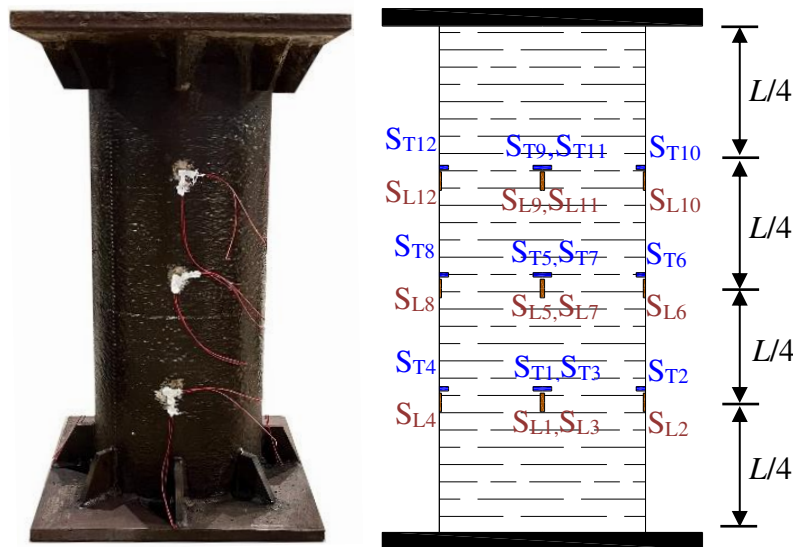


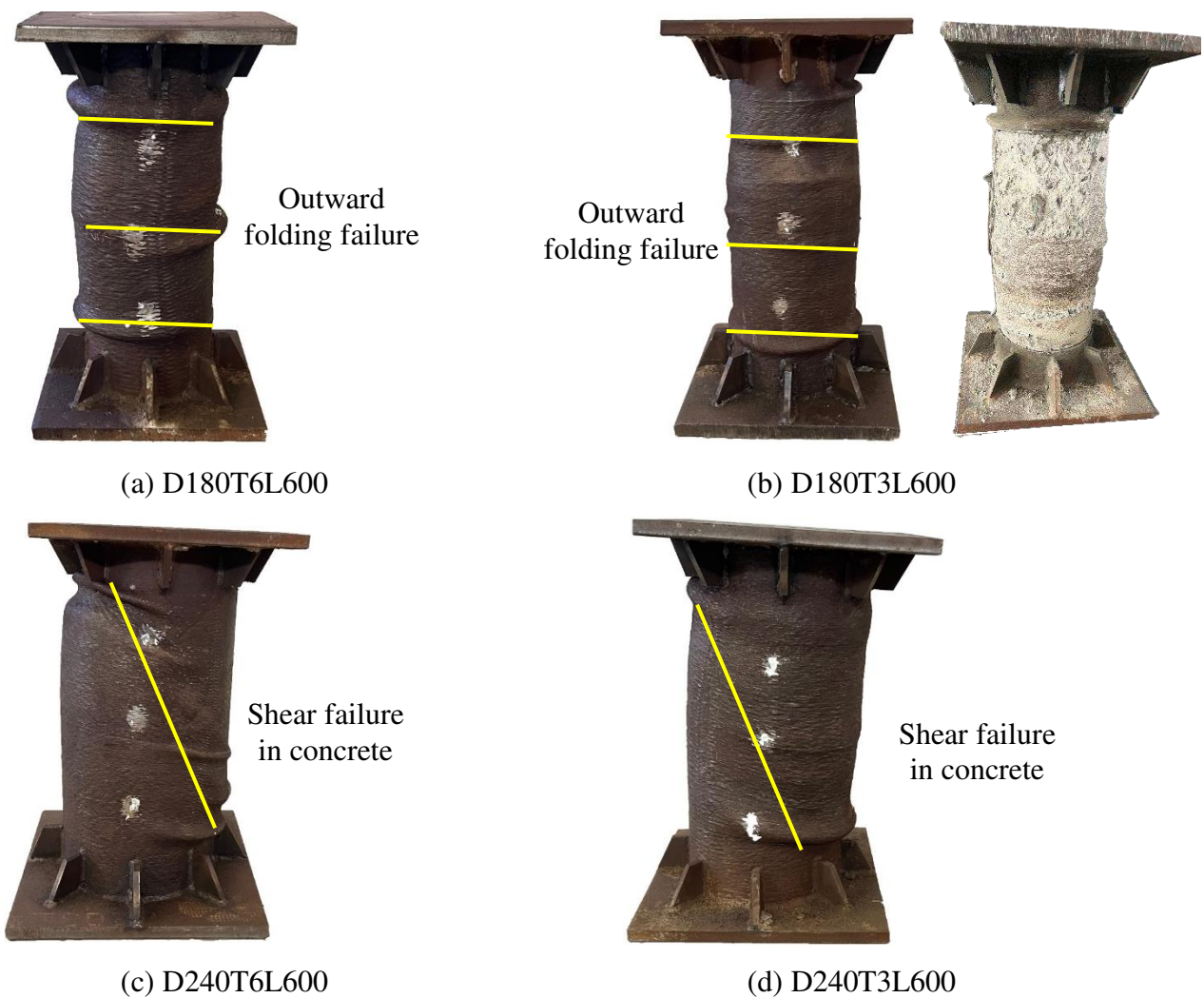
Figure 17. Arrangement of strain gauges on CFST specimens

293 5.3. Results and discussion

294 5.3.1. Failure modes and ultimate capacities

295 The failure modes of the CFST specimens are presented in Fig. 18. The failure modes of all CFST
 296 specimens involved inelastic local buckling of the WAAM steel tubes and concrete crushing. More
 297 specifically, CFST specimens D180T6L600 and D180T3L600 failed due to outward folding of the
 298 section, as shown in Figs. 18(a) and (b), while for the rest of the CFST specimens, shear failure of the
 299 inner concrete occurred, as shown in Figs. 18(c)-(i). The observed failure modes were generally similar

300 to those described by other researchers [41,47,68-71] for CFST members with conventionally produced
301 straight seam steel tubes. It should also be mentioned that, unlike for CFST members fabricated from
302 conventional steel tubes, where fracture of the steel tubes is often observed, no fracture occurred for the
303 specimens examined herein. This is attributed to the WAAM tubes being composed of continuously
304 printed 'hoop' of high ductility that were able to effectively resist the outward pressure from the confined
305 concrete, in contrast to the seam welds running along the length of traditionally fabricated tubes that act
306 as weak points. The continuous 'hoop' and the resulting absence of fracture had a positive impact on
307 the ductility of the specimens after the attainment of their ultimate load.





Shear failure
in concrete

(e) D300T6L600



Shear failure
in concrete

(f) D300T3L600



Shear failure
in concrete

(g) D300T4L1200



Shear failure
in concrete

(h) D240T4L1200



Shear failure
in concrete

(i) D180T4L1200

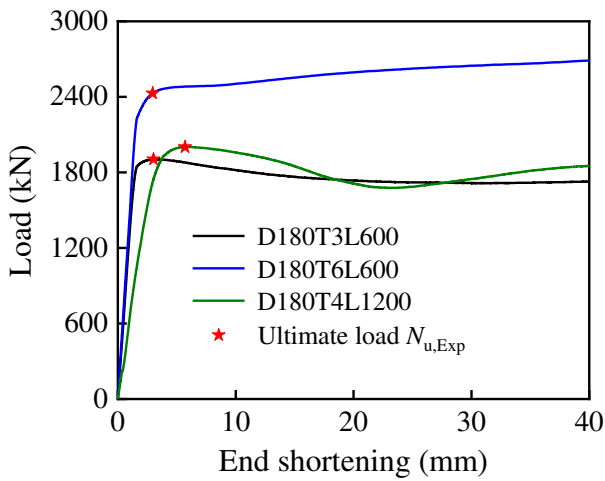
Figure 18. Failure modes of CFST specimens

308 The ultimate loads $N_{u,Exp}$ of the CFST specimens, as well as the corresponding vertical $\delta_{V,u}$ and
 309 horizontal displacements $\delta_{H,u}$ obtained in the experiments are summarised in Table 4. As expected, the

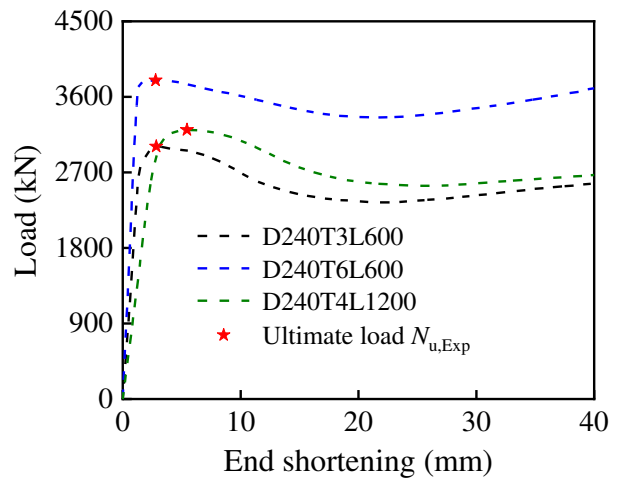
310 cross-sectional area had the most marked influence on the load-carrying capacity, with the ultimate load
 311 $N_{u,Exp}$ increasing with increasing of cross-sectional area. Note that the lateral displacement at ultimate
 312 load, which were only measured for the longer specimens (D180T4L1200, D240T4L1200 and
 313 D300T4L1200), were significantly lower than the corresponding axial shortening - see Table 4,
 314 indicating a minimal influence of global instability in the CFST experiments.

315 5.3.2. Load-end shortening curves

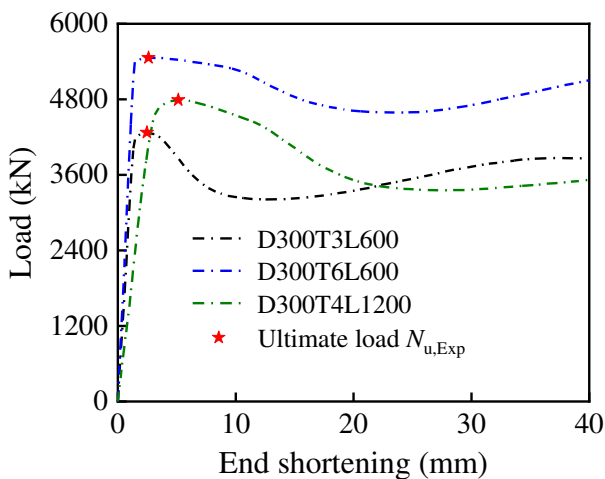
316 The load-end shortening curves of all CFST specimens obtained from the axial compression tests are
 317 illustrated in Fig. 19. The specimens exhibited a linear elastic response in the early stages of loading.
 318 This was followed by yielding of the WAAM tube, characterised by a sharp drop in stiffness but with
 319 no visible outward deformations. Finally, development of significant local buckling of the WAAM steel
 320 tube and crushing of the inner concrete led to the attainment of the ultimate load of the specimens.



(a) D180 series

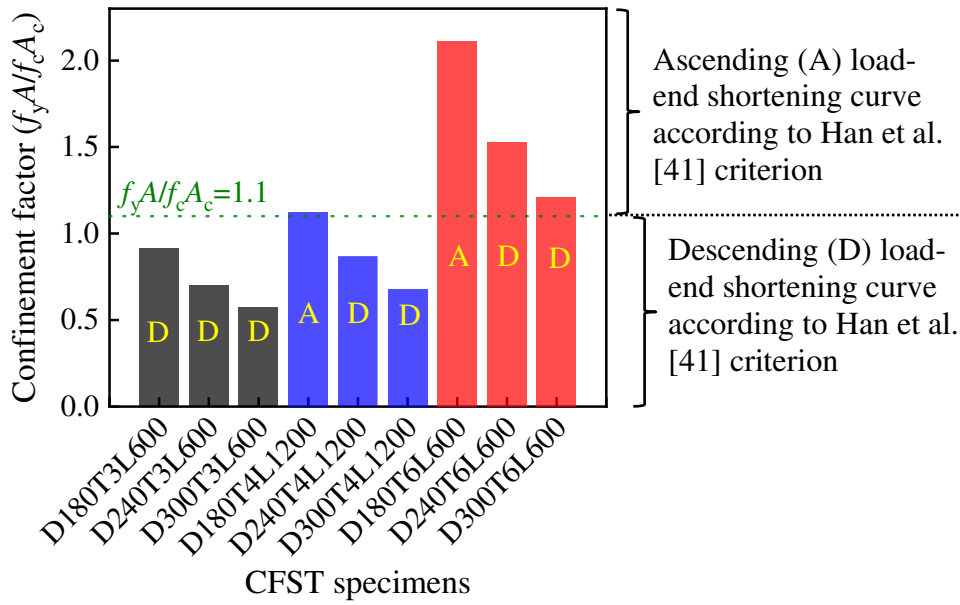


(b) D240 series

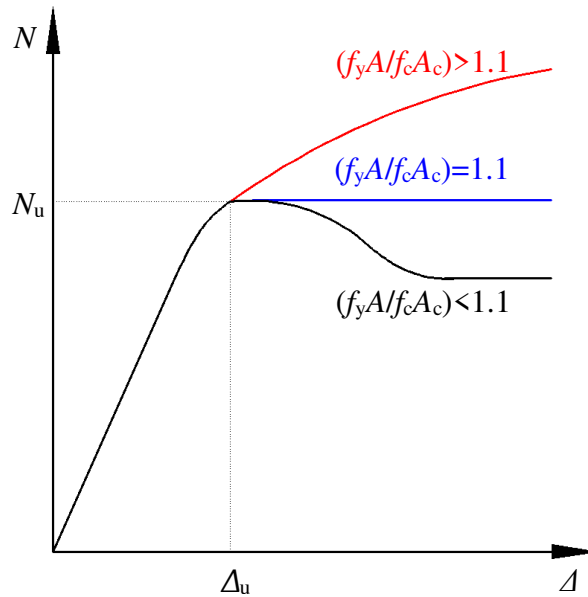


(c) D300 series

Figure 19. Load-end shortening curves of CFST specimens



(a) Confinement factors ($f_y A / f_c A_c$)



(b) Typical load-deformation ($N-\Delta$) characteristics (Han et al. [41])

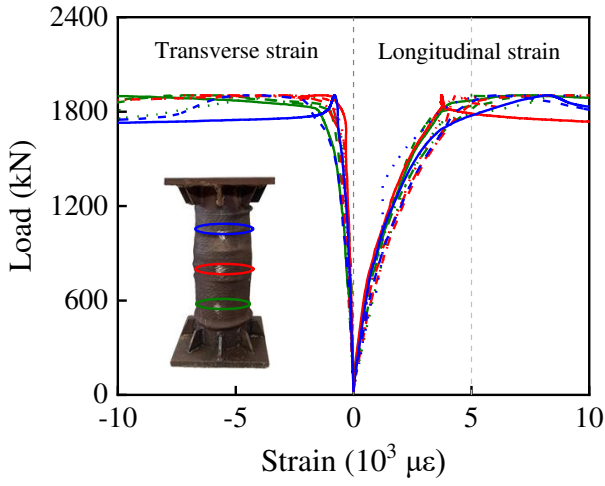
Figure 20. Comparison of confinement factors and load-deformation characteristics of CFST specimens

321 According to Han et al. [41], for conventional CFST members with diameter-to-thickness ratios
 322 within the examined range (i.e. 30-134), the profile of the load-end shortening curve is related to the
 323 confinement factor $f_y A / f_c A_c$, where f_y and A are the yield strength and cross-sectional area of the
 324 WAAM steel tube and f_c and A_c are the cylinder compressive strength and cross-sectional area of the
 325 inner concrete. The confinement factors of the specimens examined herein are presented in Fig. 20. A

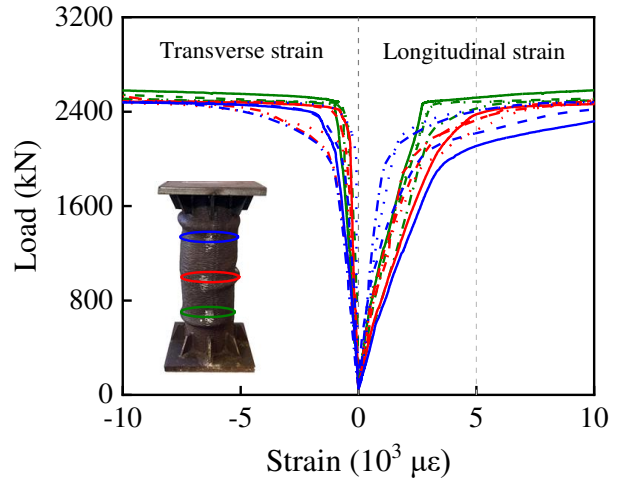
326 confinement factor greater than 1.1 corresponds to a continuously ascending load-end shortening curve
327 with increasing load, while a confinement factor less than 1.1 corresponds to a load-end shortening curve
328 that decreases after attainment of the peak load, according to the observations of Han et al. [41].
329 Otherwise, when $f_y A / f_c A_c \approx 1.1$, a plateau in the load-end shortening curve after failure is anticipated
330 [41]. It can be seen from Figs. 19 and 20 that, except for Specimens D240T6L600 and D300T6L600,
331 the load-end shortening curves of all specimens follow the anticipated trends, as described by Han et al.
332 [41]. The post-peak performance of Specimens D240T6L600 and D300T6L600 may have been
333 influenced more than others by surface undulations in the steel tube that are inherent to the WAAM
334 process.

335 5.3.3. Load-strain curves

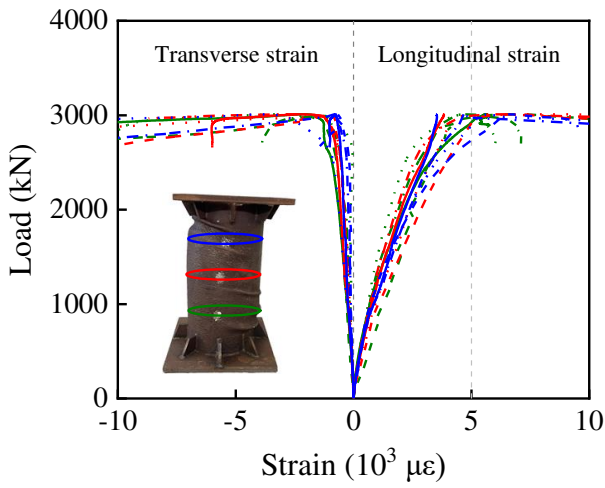
336 The load versus longitudinal and transverse strains experienced by the CFST test specimens at three
337 locations along the member length are plotted in Fig. 21. The longitudinal and transverse strains were
338 measured by the strain gauges labelled S_{L1} - S_{L12} and S_{T1} - S_{T12} , respectively – see Fig. 17, with positive
339 values indicating compression and negative values indicating tension. Note that the load–transverse
340 strain curves were employed to monitor the confinement of the concrete provided by the WAAM steel
341 tubes. The different colours of the curves in Fig. 21 represent the strains at the three different locations
342 along the specimen length. Lines of the same colour but different type represent the strains at different
343 circumferential positions at the same height. It can be seen that there is somewhat of a spread in
344 longitudinal strain readings in the early stages of loading; this is attributed to some inevitable non-
345 uniformity in loading and properties of the infill concrete, as well as the influence of the surface
346 undulations of the WAAM tubes. After the attainment of the peak load, the spread in longitudinal strain
347 readings increases further, heralding the occurrence of local buckling.



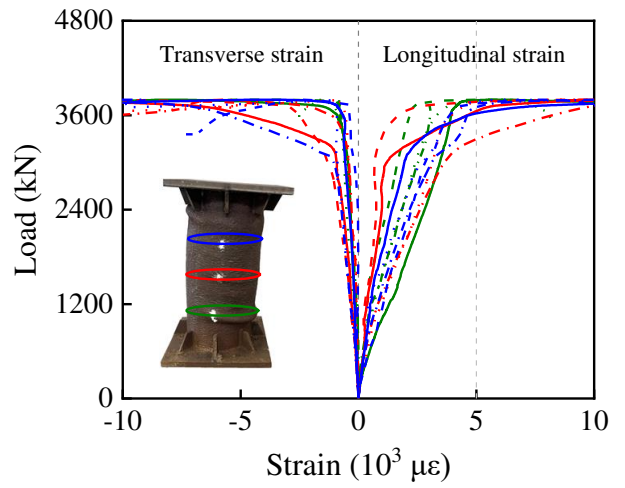
(a) D180T3L600



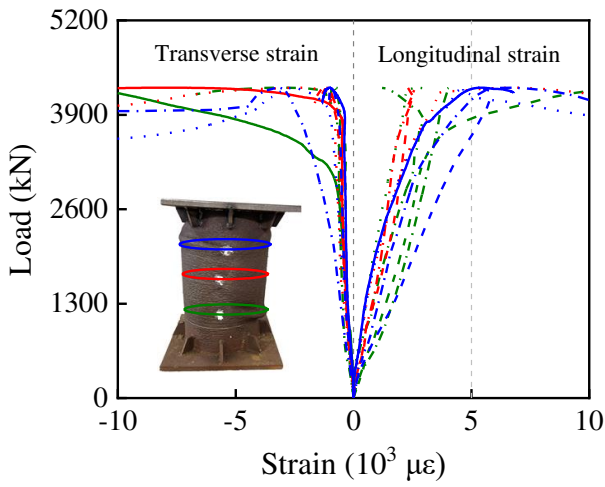
(b) D180T6L600



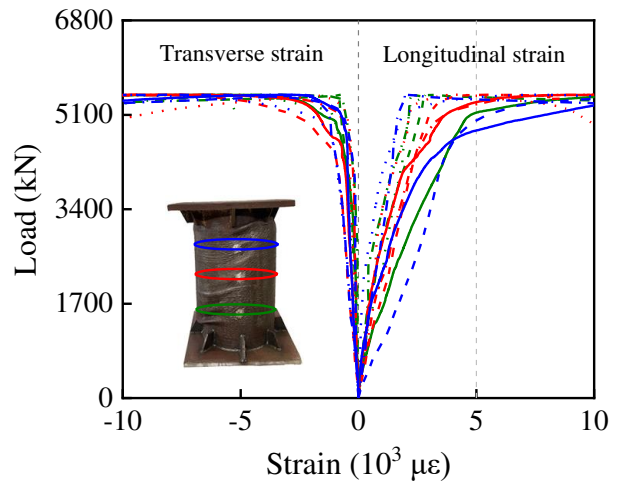
(c) D240T3L600



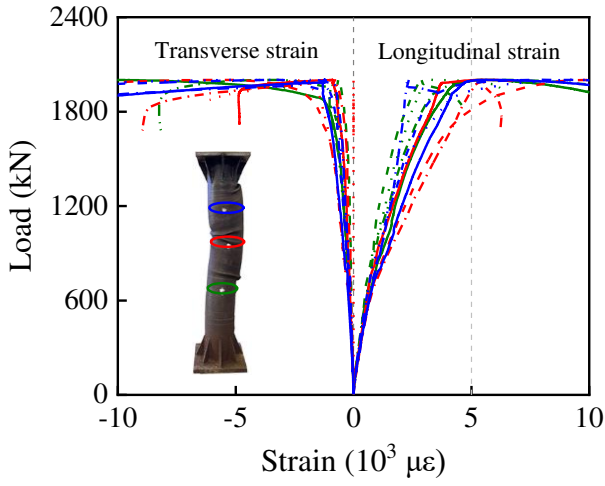
(d) D240T6L600



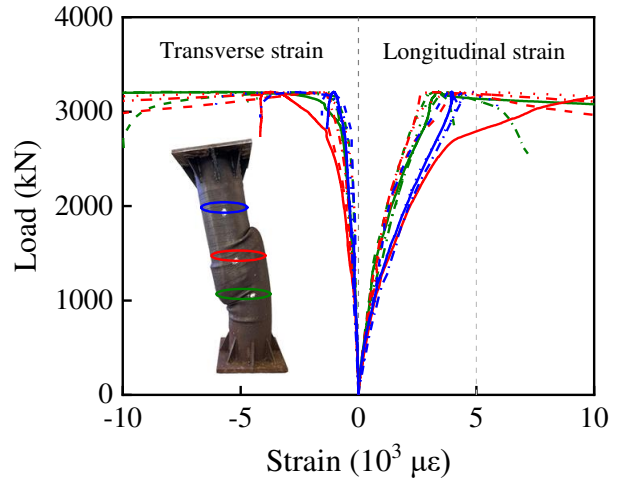
(e) D300T3L600



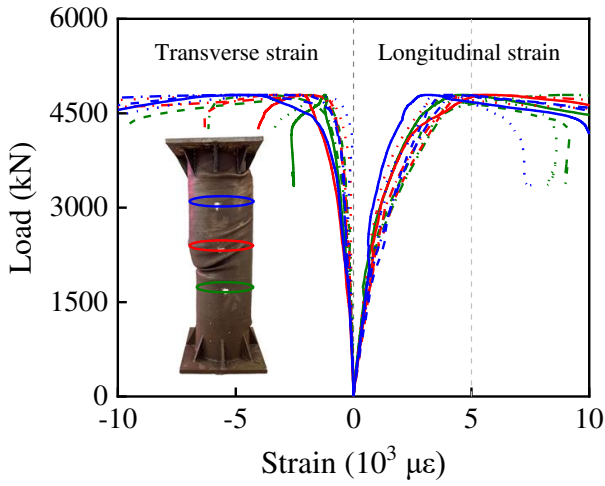
(f) D300T6L600



(g) D180T4L1200



(h) D240T4L1200



(i) D300T4L1200

Figure 21. Load–strain curves of CFST specimens

348 5.3.4. Ductility

349 To investigate the ductility of the CFST specimens, the ductility index DI [41,72] given by Equation (2)
 350 was adopted.

351
$$DI = \frac{\varepsilon_{0.85}}{\varepsilon_b} \quad (2)$$

352 In Equation (2), $\varepsilon_{0.85}$ is the axial strain in the specimen when the load falls to 85% of the ultimate load
 353 (see Fig. 22(a)) and ε_b is equal to $\varepsilon_{0.75} / 0.75$, in which $\varepsilon_{0.75}$ is the axial strain in the specimen when the
 354 load attains 75% of the axial compressive strength in the pre-ultimate stage, as shown in Fig. 22(a). It
 355 should be noted that for the specimens without a 15% decrease in ultimate load after the attainment of

356 the axial compressive strength, $\varepsilon_{0.85}$ was taken as three times the strain at their ultimate load ($3\varepsilon_u$) for
 357 the calculation of DI [73].

358 The ductility indices DI calculated using Eq. (2) for all WAAM CFST specimens are shown in
 359 Table 4. The DI values are also plotted in Fig. 22(b) against the tube diameter to wall thickness ratio
 360 D/T , and compared with corresponding DI values determined from tests on a sample of CFST members
 361 comprising conventional steel tubes [41]. The results show that the range of calculated DI values for the
 362 WAAM CFST specimens varied from 4.5 to 7.1, and were consistently higher than the DI values for the
 363 corresponding conventional CFST members; this is attributed to the high ductility of the WAAM steel
 364 tube and the fact that higher grade and less ductile concrete (C80) was used in the conventional
 365 specimens against with which the present specimens are compared.

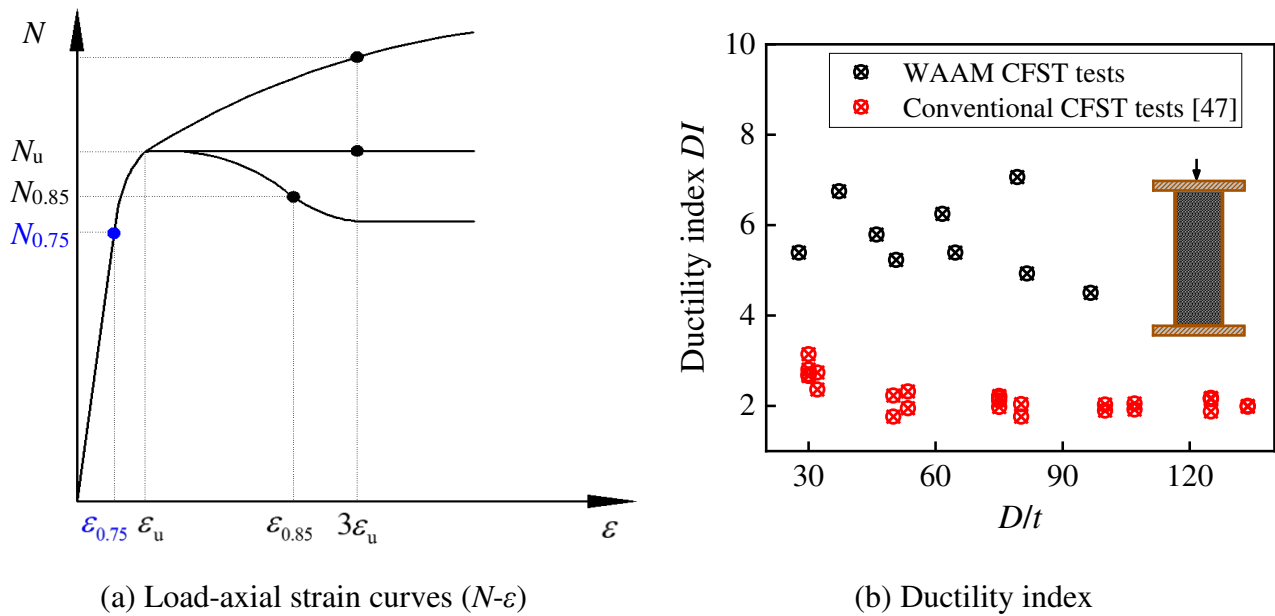


Figure 22. Load-axial strain curves and ductility indices of CFST specimens

366

Table 7 Summary of design code expressions for predicting axial compressive resistance of CFST sections

Design code	Expression	Notes
GB 50936	$N_{u,GB} = \varphi_l N_0$	$N_0 = \begin{cases} 0.9A_c f_c (1 + 2 \frac{f_y A}{f_c A_c}) & \frac{f_y A}{f_c A_c} \leq 1 \\ 0.9A_c f_c (1 + \sqrt{\frac{f_y A}{f_c A_c}} + \frac{f_y A}{f_c A_c}) & \frac{f_y A}{f_c A_c} > 1 \end{cases}$ φ_l : buckling reduction factor
AISC 360–16	$N_{u,AISC} = \begin{cases} P_{no} \left(0.658 \frac{P_{no}}{P_e} \right) & \frac{P_{no}}{P_e} \leq 2.25 \\ 0.877 P_e & \frac{P_{no}}{P_e} > 2.25 \end{cases}$	$P_{no} = \begin{cases} P_p & \text{Compact} \\ P_p - \frac{P_p - P_y}{(\lambda_r - \lambda_p)^2} (\lambda - \lambda_p)^2 & \text{Non-compact} \end{cases}$ $P_p = f_y A + 0.95 A_c f_c$; $P_y = f_y A + 0.7 A_c f_c$ λ , λ_r and λ_p : section slenderness ratio
EC4	$N_{u,EC} = \chi \left[\eta_a f_y A + (1 + \alpha_{sc}) A_c f_c \right]$	$\alpha_{sc} = \eta_b \frac{t f_y}{D f_c}$ η_a and η_b : strength parameters χ : buckling reduction factor
AS 5100	$N_{u,AS} = \alpha_c \left[\eta_2 f_y A + \left(1 + \eta_1 \frac{t f_y}{D f_c} \right) A_c f_c \right]$	η_1 and η_2 : strength parameters α_c : buckling reduction factor
ACI 318	$N_{u,ACI} = f_y A + 0.85 A_c f_c$	-
BS 5400	$N_{u,BS} = 0.95 f_y A + 0.45 A_c f_{cc}$	$f_{cc} = f_{cu} + C_1 C_2 \frac{t}{D} f_y$; C_1 and C_2 : strength parameters
AIJ 2001	$N_{u,AIJ} = 1.27 f_y A + A_c f_c$	$L_0 / D \leq 4$

Table 8 Comparisons of axial compression resistance predictions and experimental results for CFST specimens

Specimen ID	GB 50936		AISC 360–16		EC4		AS 5100		ACI 318		BS 5400		AIJ 2001	
	$\frac{N_{u,GB,m}}{N_{u,Exp}}$	$\frac{N_{u,GB,a}}{N_{u,Exp}}$	$\frac{N_{u,AISC,m}}{N_{u,Exp}}$	$\frac{N_{u,AISC,a}}{N_{u,Exp}}$	$\frac{N_{u,EC,m}}{N_{u,Exp}}$	$\frac{N_{u,EC,a}}{N_{u,Exp}}$	$\frac{N_{u,AS,m}}{N_{u,Exp}}$	$\frac{N_{u,AS,a}}{N_{u,Exp}}$	$\frac{N_{u,ACI,m}}{N_{u,Exp}}$	$\frac{N_{u,ACI,a}}{N_{u,Exp}}$	$\frac{N_{u,BS,m}}{N_{u,Exp}}$	$\frac{N_{u,BS,a}}{N_{u,Exp}}$	$\frac{N_{u,AIJ,m}}{N_{u,Exp}}$	$\frac{N_{u,AIJ,a}}{N_{u,Exp}}$
	D180T3L600	0.96	0.95	0.71	0.71	0.86	0.85	0.83	0.82	0.69	0.68	0.73	0.71	0.72
D240T3L600	0.97	0.96	0.72	0.72	0.87	0.86	0.88	0.87	0.70	0.69	0.73	0.71	0.70	0.69
D300T3L600	0.95	0.94	0.62	0.62	0.90	0.89	0.91	0.90	0.71	0.70	0.72	0.70	0.69	0.68
D180T6L600	1.12	1.09	0.84	0.82	1.04	1.01	0.99	0.97	0.84	0.82	0.99	0.96	0.95	0.92
D240T6L600	1.13	1.10	0.82	0.80	1.00	0.99	1.02	1.00	0.79	0.78	0.94	0.92	0.87	0.85
D300T6L600	1.10	1.08	0.79	0.78	1.01	0.99	1.02	1.00	0.77	0.75	0.90	0.88	0.82	0.80
D180T4L1200	0.98	0.96	0.62	0.60	0.94	0.92	0.81	0.79	0.75	0.74	0.76	0.74	0.80	0.79
D240T4L1200	0.99	0.98	0.68	0.67	0.91	0.90	0.85	0.84	0.74	0.73	0.75	0.74	0.76	0.75
D300T4L1200	0.95	0.93	0.63	0.62	0.87	0.86	0.85	0.84	0.71	0.70	0.71	0.70	0.71	0.69
Mean	1.02	1.00	0.71	0.70	0.93	0.92	0.91	0.89	0.74	0.73	0.80	0.78	0.78	0.76
CoV	0.070	0.068	0.113	0.112	0.069	0.065	0.087	0.084	0.061	0.056	0.129	0.124	0.108	0.103

371 **6. COMPARISONS AGAINST CURRENT DESIGN SPECIFICATIONS**

372 The suitability of current structural design standards for application to the studied WAAM CFST
373 elements is assessed in this section. The axial compressive strengths of the tested specimens are
374 compared against the strength predictions yielded by seven design codes, namely GB 50936 [52], AISC
375 360–16 [18], EC4 [53], AS 5100 [54], ACI 318 [55], BS 5400 [56] and AIJ [57], the design formulae
376 of which are summarised in Table 7. The average geometric properties of the specimens, as determined
377 from the laser scans or ‘Archimedes’ measurements - see Table 4, were used for the conducted
378 calculations. Considering that the the influence of the geometric undulations associated with WAAM
379 inherently feature in the effective material properties of the as-built material, two different sets of
380 material properties were considered in the design calculations: (1) the material properties from the
381 machined coupons in the 90° direction, and (2) the material properties from the as-built coupons in the
382 90° direction. For the machined case, in the absence of results for the 3 mm and 4 mm material, the
383 results for the 6 mm material were used for all comparisons. For the as-built case, the mechanical
384 properties for the corresponding nominal material thicknesses were employed (i.e. the material
385 properties of the 3 mm thick coupons were applied to the 3 mm thick CFST specimens and the material
386 properties of the 6 mm thick coupons were applied to 6 mm thick CFST specimens), as reported in Table
387 6. For the 4 mm thick CFST specimens, in the absence of 4 mm thick coupon test results, the material
388 properties of the 3 mm thick coupons were used for the calculations.

389 Comparisons between the experimental results and the strength predictions determined according
390 to the different design codes are presented in Fig. 23 and listed in Table 8. It can be observed that use
391 of the material properties obtained from the machined and as-built coupons leads to similar predictions
392 of the axial compressive strengths of the examined specimens, reflecting the similarity in the two sets
393 of material properties in the current study. As expected, use of the material properties of the as-built
394 coupons leads to slightly more safe-sided resistance predictions since the weakening effect of the
395 geometric undulations is accounted for.

396 The comparisons demonstrate that the resistance predictions of GB 50936 are the most accurate

397 with the mean and CoV values of $N_{u,GB,a} / N_{u,Exp}$ being 1.00 and 0.068. The predictions yielded by EC4
 398 and AS 5100 remain accurate and are generally safe-sided, with the mean values of $N_{u,EC4,a} / N_{u,Exp}$ and
 399 $N_{u,AS,a} / N_{u,Exp}$ being 0.92 and 0.89, respectively, and the corresponding CoV values being 0.065 and
 400 0.084, respectively. All GB 50936, EC4 and AS 5100 predictions generally lay within a $\pm 15\%$ band,
 401 as shown Fig. 23. Finally, the resistance predictions determined according to the design equations of
 402 AISC 360–16, ACI318, BS5400 and AIJ were found to be overly conservative.

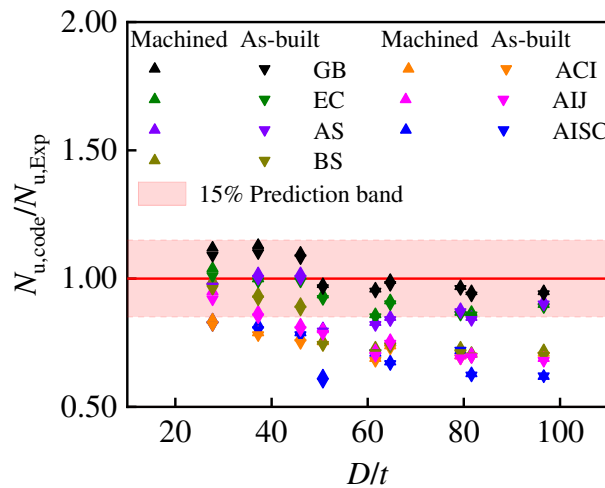


Figure 23. Comparison of resistance predictions and experimental results of CFST specimens

403 The design of WAAM CFST members will be explored further in future research, supported by the
 404 addition of numerical simulations. In particular, the influence of the surface undulations associated with
 405 the WAAM process will be studied.

406 7. CONCLUSIONS

407 An experimental investigation into the structural response of concrete-filled WAAM steel tubes has
 408 been presented in this paper. Following determination of the geometric and material properties of the
 409 WAAM steel, together with the strength of the infill concrete, the specimens were subjected to axial
 410 compression tests. The key obtained results, including the load-deformation curves and failure modes,
 411 were reported, analysed and discussed. Finally, the applicability of current design specifications to the
 412 examined members was assessed. The main findings are summarised as follows:

413 (1) The geometric properties of the WAAM steel components were determined by hand
 414 measurements, measurements based on Archimedes' principle and 3D laser scanning. Comparisons

415 revealed good correlation between the Archimedes' and 3D laser scan measurements. Overall, 3D laser
416 scanning is considered to be the most suitable method for the accurate determination of the geometry of
417 WAAM steel elements.

418 (2) Monotonic tensile coupon tests and concrete cube compression tests were conducted to obtain the
419 material properties of the WAAM steel tubes and inner concrete, respectively. Mild anisotropy was
420 observed for the WAAM steel, which was more pronounced for the thinner coupons.

421 (3) Nine concrete-filled WAAM steel tubular specimens were tested to investigate their mechanical
422 behaviour under axial compression. The experimental results demonstrated that: (i) the observed failure
423 modes are generally similar to those exhibited by CFST members comprising conventionally-produced
424 straight seam steel tubes, (ii) the correlation between the trend of the load-end shortening curves of the
425 examined specimens and their confinement factor is somewhat different to that of conventional CFST;
426 this is attributed to the surface undulations of the WAAM elements, and (iii) the ductility of the
427 examined WAAM specimens is better than that of the conventional CFST members, based on some
428 sample comparisons.

429 (4) The axial compressive strengths of the examined CFST specimens were compared against the
430 strength predictions yielded by current design specifications (i.e. GB 50936, AISC 360-16, EC4, AS 5100,
431 ACI318, BS5400 and AIJ). It was shown that, provided the weakening effect of the surface undulations is
432 taken into consideration, GB 50936, EC4 and AS 5100 offer accurate predictions of the compressive
433 strength of concrete-filled WAAM steel tubes, within a reasonable error band (i.e. $\pm 15\%$).

434 **Acknowledgements**

435 The authors would like to acknowledge the financial support from the National Natural Science
436 Foundation of China (NSFC) (Grant Number: 52078249, 52208215), the Natural Science Foundation
437 of Zhejiang Province (Grant Number: LQ22E080008) and the Centre for Balance Architecture of
438 Zhejiang University.

439 **References**

- 440 [1] Gardner L. 2023. Metal additive manufacturing in structural engineering: review, advances,
441 opportunities and outlook. *Structures*, 47, 2178–2193.
- 442 [2] ASTM. 2016. Guide for directed energy deposition of metals. F3187. West Conshohocken,
443 PA:ASTM.
- 444 [3] ASTM. 2019. Guide for Additive manufacturing–design–directed energy deposition. F3413. West
445 Conshohocken, PA:ASTM.
- 446 [4] Thompson MK, et al. 2016. Design for additive manufacturing: trends, opportunities,
447 considerations, and constraints. *CIRP Annals*, 65(2):737–760.
- 448 [5] Williams SW, Martina F, Addison AC, Ding J, Pardal G, Colegrove PA. 2016. Wire+arc additive
449 manufacturing. *Materials Science and Technology*, 32(7):641–647.
- 450 [6] Ye J, Kyvelou P, Gilardi F, Lu H, Gilbert M, Gardner L. 2021. An end–to–end framework for the
451 additive manufacture of optimized tubular structures. *IEEE Access*, 9:165476–165489.
- 452 [7] Colegrove PA, Coules HE, Fairman JL, Martina F, Kashoob T, Mamash H, Cozzolino LD. 2013.
453 Microstructure and residual stress improvement in wire and arc additively manufactured parts
454 through high–pressure rolling. *Journal of Materials Processing Technology*, 213:1782–1791.
- 455 [8] Guo X, Kyvelou P, Ye J, Teh LH, Gardner L. 2022. Experimental investigation of wire arc
456 additively manufactured steel single–lap shear bolted connections. *Thin–Walled Structures*,
457 181:110029.
- 458 [9] Guo X, Kyvelou P, Ye J, Gardner L. 2023. Experimental investigation of wire arc additively
459 manufactured steel T–stub connections. *Journal of Constructional Steel Research*, 211:108106.
- 460 [10] Guo X, Kyvelou P, Ye J, Teh LH, Gardner L. 2023. Experimental study of DED–arc additively
461 manufactured steel double–lap shear bolted connections. *Engineering Structures*, 281: 115736.
- 462 [11] Haden CV, Zeng G, Carter III FM, Ruhl C, Krick BA, Harlow DG. 2017. Wire and arc additive
463 manufactured steel: Tensile and wear properties. *Additive Manufacturing*, 16: 115–123.
- 464 [12] Kyvelou P, Huang C, Gardner L, Buchanan C. 2021. Structural testing and design of wire arc
465 additively manufactured square hollow sections. *Journal of Structural Engineering*,
466 147(12):04021218.
- 467 [13] Lange J, Feucht T, Erven M. 2020. 3D printing with steel–additive manufacturing for connections
468 and structures. *Steel Construction*, 13(3), 144–153.
- 469 [14] Laghi V, Palermo M, Gasparini G, Girelli VA, Trombetti T. 2020. Experimental results for
470 structural design of wire–and–arc additive manufactured stainless steel members. *Journal of*
471 *Constructional Steel Research*, 16:105858.

- 472 [15]Liu YY, Ye J, Yang YZ, Quan G, Zhao WJ, Zhao Y. 2023. Experimental study on wire and arc
473 additively manufactured steel double–shear bolted connections. *Journal of Building Engineering*,
474 76:107330.
- 475 [16]Müller J, Grabowski M, Müller C, Hensel J, Unglaub J, Thiele K, Kloft H, Dilger K. 2019. Design
476 and parameter identification of wire and arc additively manufactured (WAAM) steel bars for use in
477 construction. *Metals*, 9(7): 1–19.
- 478 [17]Zhao Y, Chen Y, Wang Z, Ye J, Zhao WJ. 2023. Mechanical properties, microstructural
479 characteristics and heat treatment effects of WAAM stainless–steel plate material. *Journal of*
480 *Building Engineering*, 75:106988.
- 481 [18]AISC. 2016. Specification for structural steel buildings. AISC360–16. Chicago, USA:AISC.
- 482 [19]AS. 1998. Building Code of Australia Primary Referenced Standard: Steel Structures. AS4100.
483 Homebush, Australia: AS.
- 484 [20]CEN (European Committee for Standardization). 2007. Eurocode 3: Design of Steel Structures. Part
485 1.8: Design of Joints. EN1993–1–8. Brussels, Belgium: CEN.
- 486 [21]GB (Chinese Code). 2017. Code for Design of Steel Structures. GB 50017, Beijing, China:
487 Standards Press of China.
- 488 [22]Kyvelou P, Slack H, Mountanou DD, Wade MA, Britton TB, Buchanan C, Gardner L. 2020.
489 Mechanical and microstructural testing of WAAM sheet material. *Materials and Design*,
490 192:108675.
- 491 [23]Hadjipantelis, N., Weber, B., Buchanan, C. and Gardner, L. 2022. Description of anisotropic
492 material response of wire and arc additively manufactured thin-walled stainless steel elements.
493 *Thin-Walled Structures*, 171, 108634.
- 494 [24]Huang, C, Meng X and Gardner L. 2022. Cross–sectional behaviour of wire arc additively
495 manufactured tubular beams. *Engineering Structures*, 272, 114922.
- 496 [25]Kyvelou P, Buchanan C, Gardner L. 2022. Numerical simulation and evaluation of the world’s first
497 metal additively manufactured bridge. *Structures*, 42, 405–416.
- 498 [26]Yan JJ, Chen MT, Quach WM, Yan M, Young B. 2019. Mechanical properties and cross–sectional
499 behavior of additively manufactured high strength steel tubular sections. *Thin–Walled Structures*,
500 144:106158.
- 501 [27]Al–Nabulsi Z, Mottram JT, Gillie M, Kourra N, Williams MA. 2021. Mechanical and X ray
502 computed tomography characterisation of a WAAM 3D printed steel plate for structural engineering
503 applications. *Construction and Building Materials*, 274, 121700.
- 504 [28]Huang C, Kyvelou P, Zhang R, Britton TB, Gardner L. 2022 Mechanical testing and microstructural
505 analysis of wire arc additively manufactured steels. *Materials and Design*, 216, 110544.

- 506 [29]Huang C, Kyvelou P, Gardner L. 2023. Stress–strain curves for wire arc additively manufactured
507 steels. *Engineering Structures*, 279, 115628.
- 508 [30]Silvestru VA, Ariza I, Vienne J, Michel L, Sanchez AMA, Angst U, Rust R, Gramazio F, Kohler
509 M, Taras A. 2021. Performance under tensile loading of point–by–point wire and arc additively
510 manufactured steel bars for structural components. *Materials and Design*, 205, 109740.
- 511 [31]Weber B, Meng X, Zhang R, Nitawaki M, Sagawa T, Gardner L. 2024. Tensile behaviour of
512 WAAM high strength steel material and members. *Materials and Design*, 237, 112517.
- 513 [32]Laghi V, Palermo M, Gasparini G, Trombetti T. 2020. Computational design and manufacturing of
514 a half–scaled 3D–printed stainless steel diagrid column. *Additive Manufacturing*, 36, 101505.
- 515 [33]Meng X, Weber B, Nitawaki M, Gardner L. 2023. Optimisation and testing of wire arc additively
516 manufactured steel stub columns. *Thin–Walled Structures*, 189, 110857.
- 517 [34]Bruggi M, Laghi V, Trombetti T. 2021. Simultaneous design of the topology and the build
518 orientation of wire–and–arc additively manufactured structural elements. *Computers and Structures*,
519 242, 106370.
- 520 [35]Feucht T, Waldschmitt B, Lange J, Erven M. 2022. Additive manufacturing of a bridge in situ. *Steel
521 Construction*, 15(2), 100–110.
- 522 [36]Kyvelou P, Spinasa A, Gardner L. 2024. Testing and analysis of optimised wire arc additively
523 manufactured steel trusses. *Journal of Structural Engineering, ASCE*, 150(3), 04024008.
- 524 [37]Shah IH, Hadjipantelis N, Walter L, Myers RJ, Gardner L. 2023. Environmental life cycle
525 assessment of wire arc additively manufactured structural components. *Journal for Cleaner
526 Production*, 389, 136071.
- 527 [38]Gardner L, Li J, Meng X, Huang C, Kyvelou P. 2024. I-section steel columns strengthened by wire
528 arc additive manufacturing concept and experiments. *Engineering Structures*, 306, 117763.
- 529 [39]Kyvelou P, Huang C, Li J, Gardner L. 2024. Residual stresses in steel I–sections strengthened by
530 wire arc additive manufacturing. *Structures*, 60, 105828.
- 531 [40]Han LH, Zhao XL, Yang YF, Feng, JB. 2003. Experimental study and calculation of fire resistance
532 of concrete–filled hollow steel columns. *Journal of Structural Engineering*, 129(3):346–356.
- 533 [41]Han LH, Yao GH, Zhao XL. 2005. Tests and calculations for hollow structural steel (HSS) stub
534 columns filled with self–consolidating concrete (SCC). *Journal of Constructional Steel Research*,
535 61:1241–1.
- 536 [42]Tao Z, Han LH, Wang ZB. 2005. Experimental behaviour of stiffened concrete–filled thin–walled
537 hollow steel structural (HSS) stub columns. *Journal of Constructional Steel Research*, 61:962–983.
- 538 [43]Uy B, Tao Z, Han LH. 2011. Behaviour of short and slender concrete–filled stainless steel tubular
539 columns. *Journal of Constructional Steel Research*, 67(3):360–378.

- 540 [44] Wang F, Young B, Gardner L. 2020. CFDST sections with square stainless steel outer tubes under
541 axial compression: Experimental investigation, numerical modelling and design. *Engineering*
542 *Structures*, 207, 110189.
- 543 [45] Liang QQ, Uy B, Liew JYR. 2006. Nonlinear analysis of concrete-filled thin-walled steel box
544 columns with local buckling effects. *Journal of Constructional Steel Research*, 62(6):581–591.
- 545 [46] Xiong MX, Xiong DX, Liew JYR. 2017. Axial performance of short concrete filled steel tubes with
546 high-and ultra-high-strength materials. *Engineering Structures*, 136:494–510.
- 547 [47] Yu Q, Tao Z, Wu YX. 2008. Experimental behaviour of high-performance concrete-filled steel
548 tubular columns. *Thin-Walled Structures*, 46:362–370.
- 549 [48] Song SS, Chen J, Ye J, Quan G, Wang Z, Xiao JZ. 2024. Experimental study on the interfacial bond
550 behaviour of circular concrete-filled WAAM steel tubes. *Journal of Building Engineering*,
551 82:108171.
- 552 [49] Xu F, Chen J, Jin WL. 2014. Experimental investigation of thin-walled concrete-filled steel tube
553 columns with reinforced lattice angle. *Thin-Walled Structures*, 84:59-67.
- 554 [50] Xu F, Chen J, Guo Y, Ye Y. 2019. Innovative design of the world's tallest electrical transmission
555 towers. *Proceedings of the Institution of Civil Engineers – Civil Engineering*, 172(5): 9–16.
- 556 [51] Song SS, Chen J, Quan G, Ye J, Zhao Y. 2024. Numerical analysis and design of concrete-filled
557 wire arc additively manufactured steel tube under axial compression. *Engineering Structures*,
558 301:117294.
- 559 [52] GB (Chinese Code). 2014. Technical code for concrete-filled steel tubular structures. GB 50936.
560 Beijing, China: Standards Press of China.
- 561 [53] CEN (European Committee for Standardization). 2004. Eurocode 4: Design of composite steel and
562 concrete structures–Part 1–1: General rules and rules for buildings. EN1994–1–1. Brussels,
563 Belgium: CEN.
- 564 [54] AS. 2004. Bridge design Part 6: Steel and composite construction. AS 5100. Sydney, Australia: AS.
- 565 [55] ACI. 2002. Building code requirements for reinforced concrete and commentary. ACI 318R–02.
566 Detroit, American: AIC.
- 567 [56] BS. 2000. Steel, concrete and composite bridges: code of practice for design of composite bridges
568 Part 5. BS 5400. London, British: BS.
- 569 [57] AIJ (Japanese Code). 1997. Recommendations for design and construction of concrete filled steel
570 tubular structures. AIJ. Japan: AIJ.
- 571 [58] Rhinoceros 3D, Robert McNeel & Associates, 2017.
- 572 [59] Ye J, Liu YY, Yang YZ, Wang Z, Zhao O, Zhao Y. 2023. Testing, analysis and design of wire and
573 arc additively manufactured steel bolted connections. *Engineering Structures*, 296:116939.

- 574 [60] Ibrahim A, Mahmoud E, Yamin M, Patibandla VC. 2014. Experimental study on Portland cement
575 pervious concrete mechanical and hydrological properties. *Construction and Building Materials*,
576 50:524–529.
- 577 [61] Park SB, Tia M. 2004. An experimental study on the water-purification properties of porous
578 concrete. *Cement and Concrete Research*, 34(2):177–184.
- 579 [62] Geomagic Wrap, 3D Systems Inc, 2017.
- 580 [63] GB (Chinese Code). 2010. *Metallic materials–Tensile testing–Part 1: Method of test at room*
581 *temperature*. GB/T 228.1. Beijing, China: Standards Press of China.
- 582 [64] GB (Chinese Code). 2002. *Test method for mechanical properties of ordinary concrete*. GB/T 50081.
583 Beijing, China: Standards Press of China.
- 584 [65] CEB–FIP Model Code 2010, Fib model code for concrete structures 2010, International Federation
585 Bedton (FIB), Lausanne, Switzerland, 2012.
- 586 [66] Song SS, Liu X, Chen J, Ye CH, Liu JDR, Liu CB. 2022. Compressive behaviour of corroded thin–
587 walled circular section steel stub columns. *Thin-Walled Structures*, 180:109794.
- 588 [67] Song SS, Xu F, Chen J, Qin FJ, Huang Y, Yan X. 2022. Feasibility and performance of novel
589 tapered iron bolt shear connectors in demountable composite beams. *Journal of Building*
590 *Engineering*, 53:104528.
- 591 [68] Aslani F, Uy B, Tao Z, Mashiri F. 2015. Behaviour and design of composite columns incorporating
592 compact high–strength steel plates. *Journal of Constructional Steel Research*, 107:94–110.
- 593 [69] Schneider SP. 1998. Axially loaded concrete-filled steel tubes. *Journal of Structural Engineering*,
594 124(10):1125–38.
- 595 [70] Uenaka K. 2014. Experimental study on concrete-filled elliptical/oval steel tubular stub columns
596 under compression. *Thin-Walled Structures*, 78:131–137.
- 597 [71] Uy B. 2000. Strength of concrete filled steel box columns incorporating local buckling. *Journal of*
598 *Structural Engineering*, 126(3):341–52.
- 599 [72] Ding FX, Luo L, Zhu J, Wang LP, Yu ZW. 2018. Mechanical behavior of stirrup-confined
600 rectangular CFT stub columns under axial compression. *Thin-Walled Structures*, 124:136–50.
- 601 [73] Chen ZP, Liu DY, Liang YH, Zhou J. Experimental investigation on axial compression performance
602 of spiral reinforcement ocean concrete-filled stainless steel tube columns. *Journal of Building*
603 *Structures* 2022; DOI:10.14006/j.jzjgxb.2022.0401. (in Chinese)